Journal of Molecular Structure 1235 (2021) 130223

Contents lists available at ScienceDirect

Journal of Molecular Structure

journal homepage: www.elsevier.com/locate/molstr

Theoretical and computational insight into the supramolecular assemblies of Schiff bases involving hydrogen bonding and C–H…π interactions: Synthesis, X-ray characterization, Hirshfeld surface analysis, anticancer activity and molecular docking analysis

Hina Andleeb[a,b,*], Lubna Danish[b], Shiza Munawar[b], Muhammad Naeem Ahmed[c], Imtiaz Khan[d,*], Hafiz Saqib Ali[d], Muhammad Nawaz Tahir[e], Jim Simpson[f,*], Shahid Hameed[a,*]

[a] Department of Chemistry, Quaid-i-Azam University, Islamabad-45320, Pakistan
[b] Sulaiman Bin Abdullah Aba Al-Khail – Centre for Interdisciplinary Research in Basic Science (SA-CIRBS), Faculty of Basic and Applied Sciences, International Islamic University, Islamabad, Pakistan
[c] Department of Chemistry, The University of Azad Jammu & Kashmir, Muzaffarabad 13100, Pakistan
[d] Department of Chemistry and Manchester Institute of Biotechnology, The University of Manchester, 131 Princess Street, Manchester M1 7DN, United Kingdom
[e] Department of Physics, University of Sargodha, Sargodha, Pakistan
[f] Department of Chemistry, University of Otago, P.O. Box 56, Dunedin, 9054, New Zealand

ARTICLE INFO

Article history:
Received 29 November 2020
Revised 21 February 2021
Accepted 1 March 2021
Available online 6 March 2021

Keywords:
Non-covalent interactions
Schiff base
Supramolecular assembly
Hirshfeld analysis
Electronic transitions
Anticancer activity

ABSTRACT

The present study examines the significance of various non-covalent interactions in the supramolecular assembly of (*E*)-1-(1-(4-nitrophenyl)ethylidene)-2-phenylhydrazine **1c** and (*E*)-3–bromo-*N*'-(1-phenylethylidene)benzohydrazide **2d**. The synthesized compounds were fully characterized by spectroscopic methods and single crystal X-ray diffraction analysis. The topology of the supramolecular assemblies was controlled by various non-covalent interactions including classical hydrogen bonding, C–H…π and Br…Br interactions which were examined in detail using several theoretical methods and DFT calculations. The optimized geometric parameters of compounds **1c** and **2d** were calculated using density functional theory (DFT/B3LYP) quantum chemical method with the 6–311++*G*(d,p) basis set using the crystallographic coordinates. Additionally, fragments contributing to the HOMO and LUMO molecular orbitals were investigated at the same level of theory. The nature and various types of intermolecular interactions in the crystal structures was also investigated by Hirshfeld surface analysis. The synthesized Schiff bases were also studied for their potential as drugs and physicochemical properties. Bioevaluation against four cancer cell lines (NCI-H460, NCI-H460/Bcl-2, MDA-MB-231 and MCF-7) showed that compound **1c** was a more potent inducer of toxicity compared to **2d**. The putative binding modes of the bioactive Schiff bases were investigated using molecular docking tools and the results revealed that both the inhibitors were stabilized in the active pocket of the enzyme *via* the formation of various interactions with the key amino acid residues.

1. Introduction

The construction of solid-state architectures utilizing purely organic molecules has witnessed a tremendous growth in supramolecular chemistry and crystal engineering, and the investigation of such self-assembly processes has fueled much research in this active area of research [1,2]. These systems mainly rely upon non-covalent interactions (*i.e.*, hydrogen bonding, π…π interactions, C–H…π interactions, and van der Waals interactions) and this underpins their interesting applications in the use of molecular recognition and complex biological systems [3-6] showing their diverse utility as a powerful tool for the construction of supramolecular architectures [7,8]. Among them, nonconventional C–H/X (X = O, N, S and π electrons) hydrogen bonding [9-13] has gained immense attention due to their ability to build supramolec-

* Corresponding author.
E-mail addresses: hina.andleeb@iiu.edu.pk (H. Andleeb), imtiaz.khan@manchester.ac.uk (I. Khan), jsimpson@alkali.otago.ac.nz (J. Simpson), shameed@qau.edu.pk (S. Hameed).

https://doi.org/10.1016/j.molstruc.2021.130223
0022-2860/

ular structures [14–19], biological structures [20–24] and anion receptors [25–28]. Inter- and intra-molecular hydrogen bonding have been employed extensively in the generation of complex organized systems due to the reversibility, specificity, directionality and cooperativity of such interactions [29]. Among the weak hydrogen bonds, C–H…π interactions are of considerable significance displaying several unique features that have impacts on chiral recognition, polymer chemistry, coordination chemistry, biochemistry, and the structures of DNA and proteins [30]. In view of these significant applications, and as a continuation of our work in this area [31], it is of much interest to explore the role of non-covalent interactions in new classes of compounds forming supramolecular architectures. Hence, in the present report, we showcase the synthesis and X-ray characterization of two Schiff bases namely (*E*)−1-(1-(4-nitrophenyl)ethylidene)−2-phenylhydrazine **1c** and (*E*)−3–bromo-*N*′-(1-phenylethylidene)benzohydrazide **2d**. The detailed description of the crystal packing and supramolecular assemblies driven by hydrogen bonding, C–H…π and Br…Br interactions is reported. Further insights into these intermolecular interactions were obtained using Hirshfeld surface analysis. Moreover, the biological applications of the synthesized compounds were tested against four human cancerous cell lines, i.e.; NCI-H460, NCI-H460/Bcl-2, MDA-MB-231 and MCF-7. In addition, molecular docking analysis was performed to elucidate the putative binding modes of the Schiff bases.

2. Experimental

2.1. Chemicals and instrumentation

Reagents and solvents used for the synthesis of compounds were purchased from Sigma-Aldrich, Merck, Alfa Aesar, and were used without any further purification. All the reagents used were of analytical grade. All reactions were carried out using oven-dried glassware. All the reactions were monitored using pre-coated silica gel ($60F_{254}$ 0.2 mm) TLC plates from Merck (Germany). The product spots were visualized under UV light at 254 nm. Melting points were recorded on a Gallenkamp melting point apparatus (MPD) in open capillaries and are uncorrected. Infra-red (IR) spectra were recorded on a Schimadzu Fourier Transform Infra-Red Spectrophotometer model 270 using the ATR (Attenuated total reflectance) facility. NMR spectra were recorded on a Bruker AV300 spectrometer at room temperature. ^{1}H and ^{13}C NMR spectra were referenced to external tetramethylsilane *via* the residual protonated solvent (^{1}H) or the solvent itself (^{13}C). Chemical shifts are quoted in parts per million (ppm). For DMSO–d_6, the shifts are referenced to 2.50 ppm for ^{1}H NMR and 39.52 ppm for ^{13}C NMR spectroscopy. Coupling constant (*J*) values are reported to the nearest 0.5 Hz. High-resolution mass spectra were recorded on a Micromass LCT electrospray ionization mass spectrometer operating at a resolution of 5000 full width half height.

2.2. Synthesis

2.2.1. Preparation of (E)−1-(1-(4-nitrophenyl)ethylidene)−2-phenylhydrazine (**1c**)

To a stirred solution of phenylhydrazine (1 mmol) in ethanol (2 mL) at 0 °C was added 4′-nitroacetophenone (1 mmol) followed by glacial acetic acid (0.5 mL). The reaction mixture was stirred at 0–15 °C for 30 min. The reaction progress was monitored by thin layer chromatography (TLC) at regular intervals. After completion of the reaction, the mixture was concentrated *in vacuo*. The crude solid was filtered off, washed with water and recrystallized from 80% EtOH/H_2O to afford **1c** as red crystals in 88% yield [32]. m.p. 145–148 °C; FTIR (ATR, cm^{-1}): 3300 (N–H), 1597 (*C* = *N*), 1550 (*N* = *O* stretch); ^{1}H NMR (300 MHz, DMSO–d_6) (δ/ppm): 9.16 (1H, s), 8.37 (2H, d, *J* = 8.4 Hz), 7.98 (2H, d, *J* = 8.4 Hz), 7.20 (2H, d, *J* = 7.8 Hz), 6.88–6.84 (1H, m), 6.79–6.72 (2H, m), 3.56 (3H, s); ^{13}C NMR (75 MHz, DMSO–d_6) (δ/ppm): 146.74, 144.70, 142.80, 133.82, 129.21, 126.09, 123.90, 120.28, 112.78, 15.91; HRMS (ESI +ve): exact mass calculated for $C_{14}H_{14}N_3O_2$ $[M + H]^+$: 256.0851; found, 256.0844.

2.2.2. Preparation of (E)−3–bromo-N′-(1-phenylethylidene)benzohydrazide (2d)

Step 1. To a stirred solution of 3-bromobenzoic acid **2a** (0.02 mol) in ethanol (25 mL) was added concentrated sulfuric acid (few drops) and the reaction mixture was heated to reflux. The progress of the reaction was monitored by TLC at regular intervals. After completion of the reaction (4 h), the mixture was concentrated *in vacuo*. The crude mixture was dissolved in ethyl acetate and washed with 10% aqueous sodium bicarbonate (2 × 25 mL). The organic layer was dried (Na_2SO_4), filtered and concentrated *in vacuo* to afford ester **2b** which was used in the next step without further purification.

Step 2. To a stirred solution of ethyl 3-bromobenzoate **2b** (0.01 mol) in ethanol (15 mL) was added hydrazine hydrate (80%, 0.08 mol). The resulting mixture was heated at reflux and progress was monitored by TLC at regular intervals. After completion of the reaction (5 h), the mixture was concentrated *in vacuo*. The crude solid was filtered off, washed with cold water, and recrystallized from 80% EtOH/H_2O to afford 3-bromobenzohydrazide **2c** [33].

Step 3. To a stirred solution of 3-bromobenzohydrazide **2c** (10 mmol) in ethanol (15 mL) was added acetophenone (11 mmol) followed by glacial acetic acid (0.5 mL). The resulting mixture was heated at reflux and the progress was monitored by TLC at regular intervals. After completion of the reaction (30 min), the mixture was concentrated *in vacuo*. The crude solid was filtered off, washed with cold water, and recrystallized from ethanol to afford (*E*)−3–bromo-*N*′-(1-phenylethylidene)benzohydrazide **2d** as transparent crystals in 85% yield [33]. m.p. 215–219 °C; FTIR (ATR, cm^{-1}): 3300 (N–H), 1597 (*C* = *N*), 1550 (*N* = *O* stretch); ^{1}H NMR (300 MHz, DMSO–d_6) (δ/ppm): 10.94 (1H, s), 8.06 (1H, s), 7.87–7.80 (2H, m), 7.77–7.51 (2H, m), 7.48–7.35 (4H, m), 2.38 (3H, s); ^{13}C NMR (75 MHz, DMSO–d_6) (δ/ppm): 180.75, 162.99, 156.89, 138.46, 136.76, 134.66, 131.03, 130.06, 128.84, 127.55, 126.96, 122.04, 15.26; HRMS (ESI +ve): exact mass calculated for $C_{15}H_{14}BrN_2O$ $[M + H]^+$: 317.0211; Found, 317.0202.

2.3. Crystal growth development

Single crystals of compounds **1c** and **2d** suitable for X-ray diffraction analysis were grown at room temperature from ethanol as the solvent.

2.4. X-ray structure determination

Diffraction data for the compounds were collected at 296(2) K for **1c** and at 293(2) K for **2d** using Mo-Kα radiation (λ = 0.71073 Å) on a Bruker Kappa APEXII CCD diffractometer, processed using APEX2 and SAINT [34] with multi-scan absorption corrections applied using SADABS [35]. The structures were solved by direct methods (SHELXS-97) [36] and refined using full-matrix least-squares procedures with SHELXL-2018 [37] and TITAN2000 [38]. All non-hydrogen atoms were refined anisotropically and hydrogen atoms were placed in calculated positions with their thermal parameters refined isotropically with U_{eq}(H) 1.2U_{eq}(N/C). Molecular plots and packing diagrams were drawn using Mercury [39] and additional metrical data were calculated using PLATON [40]. Tables were prepared using WINGX [41]. Details of the X-ray measurements and crystal data for the compounds are given in Table 1. Crystals of **2d** were not of high quality and this is

Table 1
Crystal data and structure refinement for **1c** and **2d**

Compound	**1c**	**2d**
Empirical formula	$C_{14}H_{13}N_3O_2$	$C_{15}H_{13}BrN_2O$
Formula weight	255.27	317.18
Temperature (K)	296(2)	293(2)
Wavelength (Å)	0.71073	0.71073
Crystal system	Triclinic	Orthorhombic
Space group	P −1	P b c a
a (Å)	8.2765(4)	6.9087(14)
b (Å)	10.7242(4)	7.7682(13)
c (Å)	16.4881(7)	51.548(9)
α (°)	72.489(2)	90
β (°)	80.039(2)	90
γ (°)	68.411(2)	90
Volume (Å^3)	1294.53(10)	2766.5(9)
Z	4	8
D_{calc} (Mg/m^3)	1.310	1.523
Absorption coefficient (*μ*, mm^{-1})	0.091	2.965
F(000)	536	1280
Crystal size(mm^3)	0.420 × 0.340 × 0.280	0.380 × 0.200 × 0.180
Theta range for data collection (°)	2.176 to 27.530	1.580 to 26.999
Index ranges	−10<=*h*<=10, −13<=*k*<=13, −21<=*l*<=21	−8<=*h*<=8, −9<=*k*<=7, −64<=*l*<=65
Reflections collected	21,473	19,909
Independent reflections	5931 [R(int) = 0.0354]	3012 [R(int) = 0.0705]
Completeness to theta = 25.242°	99.9%	100.0%
Refinement method	Full-matrix least-squares on F^2	Full-matrix least-squares on F^2
Data/restraints/parameters	5931 / 0 / 378	3012 / 0 / 174
Goodness-of-fit on F^2	0.946	1.198
Final R indices [$I > 2\sigma(I)$]	R1 = 0.0484, wR2 = 0.1329	R1 = 0.1142, wR2 = 0.2181
R indices (all data)	R1 = 0.0754, wR2 = 0.1570	R1 = 0.1609, wR2 = 0.2338
Extinction coefficient	0.023(3)	0.0024(5)
Largest difference peak and hole (e Å^{-3})	0.193 and −0.168	0.659 and −0.902
CCDC reference number	2,019,512	984,718

reflected in the final R index, R1 = 11.43%. Despite this the structure solved and refined without difficulty and the poorer quality of the data is reflected in the residuals on all of the reported parameters.

2.5. Computational details

Density functional theory (DFT) designates the physicochemical properties of various compounds in a precise and concise way while presenting a balance between accuracy and computing economy [42]. In the present project, all calculations were carried out using the Gaussian 09 software package [43]. The geometric parameters and the frequencies were computed in the gas phase by DFT with the Becke's three-parameter and the Lee-Yang-Parr (B3LYP) hybrid functional using the 6–311++*G* (d,p) basis sets including the Grimme dispersion correction (D3) [44]. The thermodynamic calculations were performed using the B3LYP/6–311++*G* (d,p) level of DFT theory in the gas phase and the effect of temperature on the results was calculated using the Moltran software [45]. The frequency calculations have been performed for both compounds using same level of DFT at the standard temperature of 298.15 K and a standard pressure of 1 atm. The title compounds have all positive normal mode frequencies which shows that both compounds are at local minima. The frontier molecular orbital (FMO's) analysis, other reactivity descriptors and electrostatic potential maps were computed at the same DFT level. Furthermore, the description of non-covalent interactions with reduced density gradient (RDG) analysis [46] is presented using Multiwfn software [47] and visualized by a visual molecular dynamic program (VMD) [48].

2.6. Molecular docking and physicochemical properties

Molecular docking studies were performed using Autodock Vina (ver. 1.5.6) [49]. For this purpose, the crystal structure of EGFR (PDB: 2GS6) was retrieved from protein data bank. The co-crystallized ligand and water molecules were removed, and the protein was converted to pdbqt format using Autodock Tools [50]. The structures of ligands **1c** and **2d** were sketched using Chemdraw and were converted to 3D format by Openbabel (ver. 2.3.1) [51]. PDBQT files were prepared in MGL Tools [50]. The other parameters were left as default. Finally, the conformations with the most favorable binding free energies were selected for the analysis of the interactions between the target enzyme and the inhibitors. PyMOL version 1.8.8.2 [52] and Chimera 1.6 software [53] were used for 3D molecular graphics, structural alignments, and visualizations. Physicochemical properties were calculated using SwissADME [54].

2.7. Maintenance of cell culture

Human cancerous cell lines NCI-H460 and NCI-H460/Bcl-2 (non-small cell lung cancer), MDA-MB-231 and MCF-7 (Breast cancer) were gifted from Peter Scheurich's Lab in Stuttgart, Germany. All cell lines were cultured in RPMI-1640 (Gibco) medium supplemented with 5% Fetal Bovine Serum (FBS) and 1% PenStrep (penicillin and streptomycin). The culture was kept in humidified incubator at 37 °C with 5% CO_2. Cell cultures were checked regularly for mycoplasma to ensure the absence of any contamination.

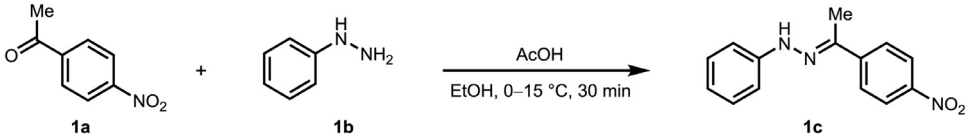

Scheme 1. Synthesis of (*E*)−1-(1-(4-nitrophenyl)ethylidene)−2-phenylhydrazine **1c**.

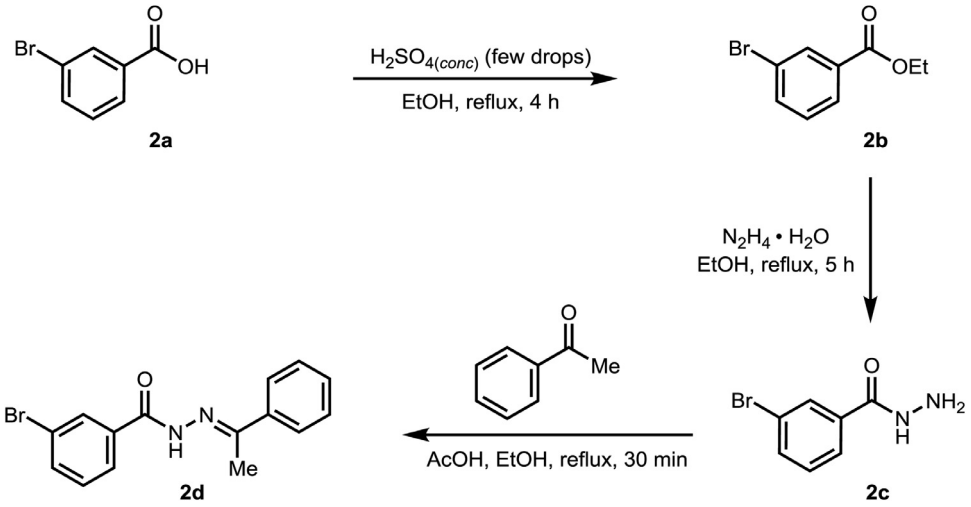

Scheme 2. Synthesis of (*E*)−3−bromo-*N*'-(1-phenylethylidene)benzohydrazide **2d**.

2.8. Cytotoxicity assays

A day prior to experiments, cells were counted and 15,000 cells/well were seeded in 96-well plates. Next day cells were stimulated with serial dilutions of both compounds (0–100 μM). After 24 h, media were removed, cells were washed with PBS and adherent (living) cells were stained with crystal violet for 15 min at room temperature. Plates were washed gently to remove excessive dye and dried overnight. 50 µL Methanol (50 μL per well) was added and the absorbance was measured in a microplate reader at 550 nm. All the values were normalized to the values from unstimulated wells.

3. Results and discussion

3.1. Synthetic chemistry

Schiff bases were prepared *via* the condensation reaction of phenylhydrazine or 3-bromobenzohydrazide with corresponding acetophenones using glacial acetic acid as illustrated in Schemes 1 and 2 [33,55]. (*E*)−3−bromo-*N*'-(1-phenylethylidene)benzohydrazide (**2d**) was prepared in three steps starting from commercially available 3-bromobenzoic acid **2a**. Acid-catalyzed esterification produced ethyl 3-bromobenzoate **2b** [33] which on hydrazination using hydrazine hydrate (80%) in ethanol furnished the desired 3-bromobenzohydrazide **2c** [33]. The condensation reaction of 3-bromobenzohydrazide **2c** with acetophenone gave the desired (*E*)−3−bromo-*N*'-(1-phenylethylidene)benzohydrazide (**2d**) in 85% yield. Both the title structures (**1c** and **2d**) were fully characterized by spectroscopic and X-ray crystallographic methods.

3.2. X-ray crystallography

A search of the Cambridge structural database version 5.41 November 2019 with 1 update March 2020 [56] for (*E*)−1-(1-(4-nitrophenyl)ethylidene)−2-phenylhydrazine **1c** gave no hits. In contrast searching for (*E*)−1-benzylidene-2-phenylhydrazine without substituents on either of the benzene rings yielded an extensive 52 hits. Limiting potential substituents to the *N*-bound ring reduced the hits significantly to 4 unique molecules. These included (*E*)−1-phenyl-2-(1-phenylethylidene)hydrazine itself [57]. Other substituents on the N-bound benzene ring were limited to NH_2 [58] and three separate reports of molecules with OH substituents [59-61], each in the 2-position of the aromatic ring. The final hit, (*E*)−1-(1-(naphthalen-2-yl)ethylidene)−2-phenylhydrazine [62] was the naphthalene analogue of the phenol derivatives.

Similarly, a search for (*E*)−3−bromo-*N*'-(1-phenylethylidene)benzohydrazide **2d**, gave no hits, whereas the search for (*E*)−3−bromo-*N*'-(1-phenylethylidene)benzohydrazide without substituents on either of the benzene rings yielded 53 hits. Further limitation of substituents to the benzene ring adjacent to the *C* = *O* group again reduced the hits significantly, in this case to only two unique molecules. (*E*)−3−bromo-*N*'-(1-phenylethylidene)benzohydrazide itself [63] and two reports of 1-(2-aminobenzoylhydrazono)−1-phenylethane [64,65].

3.2.1. Molecular structures of **1c** and **2d**

The structures of the two title compounds **1c** and **2d** are shown in Schemes 1 and 2 with their crystallographic ally determined molecular structures shown in Fig. 1 and 2, respectively.

Compound **1c** crystallizes with two unique molecules, M1 and M2, in the triclinic unit cell, Fig. 1. In M1, the H-atoms on the C18 methyl group are disordered over two sites with occupancies of 52(7) and 48(7)%, respectively. In M2, the C atoms of the N21 bound phenyl ring and their associated atoms are also disordered over two sites with an occupancy ratio 58(3):42(3). The two disorder components of these phenyl rings are inclined to one another by 2(1)°. Neither of the unique molecules are entirely planar with the outer phenyl and nitrobenzene rings inclined to one another by 8.95(11)° in M1 and 14.5(6)° in M2. Also the nitro substituents are inclined to their phenyl rings by 3.6(2)° for M1 and 4(1)° for M2. The ethylidene-hydrazine segments of both molecules are also

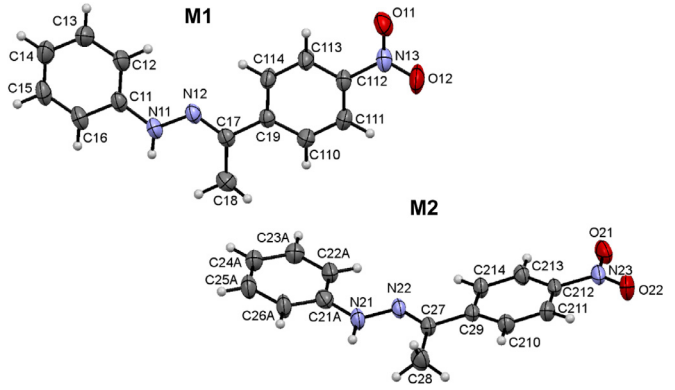

Fig. 1. The asymmetric unit of **1c** with ellipsoids drawn at the 30% probability level and the **M1** and **M2** molecules identified by leading 1 and 2 characters in the numbering schemes. For clarity only the major disorder components of the H-atoms on the C18 methyl group of **M1** and the N21 bound benzene ring of **M2** are shown.

planar with *rms* deviation of fitted atoms of 0.0022 Å for M1 and 0.0018 Å for M2.

In contrast, compound **2d** crystallizes with a single molecule in the orthorhombic unit cell. Again the molecule is not planar with an angle of 54.8(3)° between the peripheral bromo–benzene and phenyl rings with the bromo–substituent 0.110 Å (13) from the ring plane. However, the (*Z*)-*N*'-ethylideneformohydrazide section of the molecule is reasonably planar with an *rms* deviation of the 6 fitted atoms of 0.0713 Å.

3.2.2. Crystal packing of ***1c***

In the crystal of **1c** O21 acts as a bifurcated acceptor with N21-H21N…O21 and C26A-H26A…O21 enclosing R^1_2 ring motifs that form chains of M1 molecules along the *b* axis direction. These chains are linked to M1 molecules by C25A-H25A…O12 hydrogen bonds forming sheets of M1 and M2 molecules in the *bc* plane, Fig. 3.

Atom O11 of M1 also acts as a bifurcated acceptor forming N1-H11…O11 and C16-H16…O11 hydrogen bonds enclosing R^1_2 ring motifs. These contacts form chains of M1 molecules along the *ab* diagonal, Fig. 4.

An unusual feature of the packing of **1c** is the presence of three inversion related C–H…π contacts. Pairs of M1 molecules form dimers along *a* through C18-H18A…Cg5 contacts (1-x, 1-y, -z), Fig. 5. Dimers of M2 molecules also form along *a*, but in this instance the dimers result from pairs of inversion related C211-H211…Cg1 and C28-H28A…Cg2 contacts (1-x, -y, 1-z), Fig. 6. Cg5, Cg1 and Cg2 are the centroids of the C19—C114, C21A—C26A and C29—C214 rings, respectively. Overall, these contacts combine to stack the molecules along the *a* axis direction, Fig. 7. Hydrogen bonds for **1c** are shown in Table 2.

Table 2
Hydrogen bond distances (Å) and angles (°) for **1c**

D-H…A	d(D-H)	d(H…A)	d(D…A)	<(DHA)
N(11)-H(11 N)…O(11)#1	0.86	2.42	3.2142(19)	153
C(16)-H(16)…O(11)#1	0.93	2.50	3.321(3)	148
C(25A)-H(25A)…O(12)#1	0.93	2.50	3.212(5)	134
C(18)-H(18A)… Cg5#2	0.96	3.301	3.937(2)	126
C(28)-H(28A)… Cg2#3	0.96	3.114	3.914(2)	142
C(211)-H(211)… Cg1#3	0.93	3.552	4.214(3)	130

Symmetry transformations used to generate equivalent atoms:.
#1 x-1, *y* + 1, z, #2 1-x, 1-y, -z, #3 1-x, -y, 1-z. Cg5, Cg1 and Cg2 are the centroids of the C19—C114, C21A—C26A and C29—C214 rings, respectively.

Table 3
Hydrogen bond distances (Å) and angles (°) for **2d**

D-H…A	d(D-H)	d(H…A)	d(D…A)	<(DHA)
N(1)-H(1)…O(1)#1	0.86	2.19	2.984(10)	153
C(15)-H(15)…N(2)#2	0.93	2.73	3.539(13)	146
C(11)-H11…Cg2#3	0.93	2.93	3.807(12)	158

Symmetry transformations used to generate equivalent atoms:.
#1 -*x* + 1/2, y-1/2, z #2 -*x* + 1/2, *y* + 1/2, z, #3 −1/2-x, −1/2 + *y*, z. Cg2 is the centroid of the C10…C15 ring.

3.2.3. Crystal packing of ***2d***

In the crystal of **2d** classical N1-H1…O1 hydrogen bonds, supported by weaker C15-H15…N2 contacts, form chains of molecules along the *b* axis direction, Fig. 8.

Chains also form along *b* as a result of C11-H11…π contacts to the centroid of the C10—C15 phenyl ring, Fig. 9.

Close Br…Br contacts form molecular dimers and, in the overall packing arrangement, link adjacent pairs of stacked molecules along the *c* axis direction, Fig. 10. The molecules of **2d** stack along the *a* axis. Hydrogen bonds for **2d** are shown in Table 3.

3.3. Hirshfeld surface analysis

Further details of the intermolecular interactions in **1c** and **2d** were obtained using Hirshfeld surface analysis [66] with Hirshfeld surfaces and two-dimensional fingerprint plots generated with *Crystal Explorer* [67]. Figs. 11 and 12 show the Hirshfeld surfaces for opposite faces of the asymmetric units of **1c** and **2d.** For **1c** the bold red circles correspond to N–H…O and C–H…O hydrogen

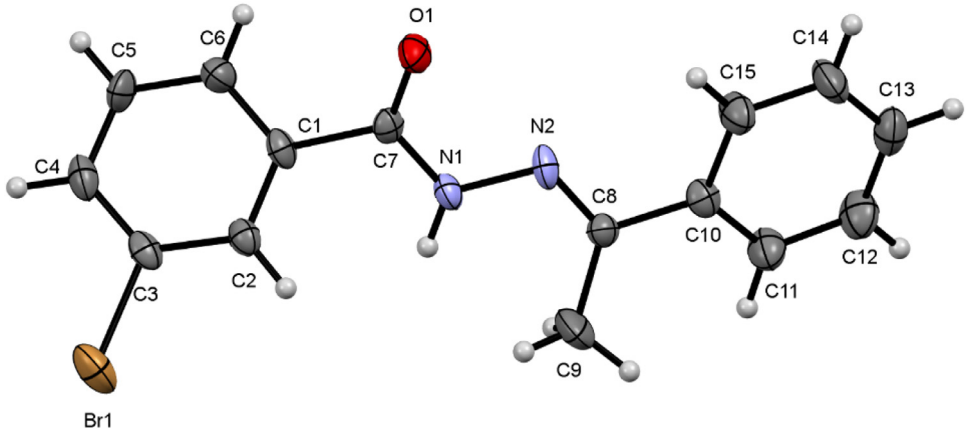

Fig. 2. The molecular structure of **2d** with ellipsoids drawn at the 30% probability level.

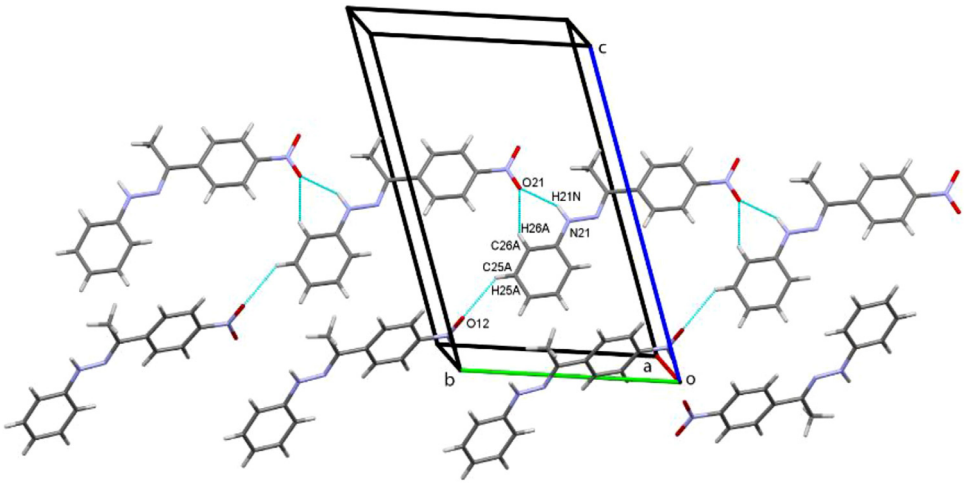

Fig. 3. Sheets of M1 and M2 molecules of **1c** formed in the *bc* plane.

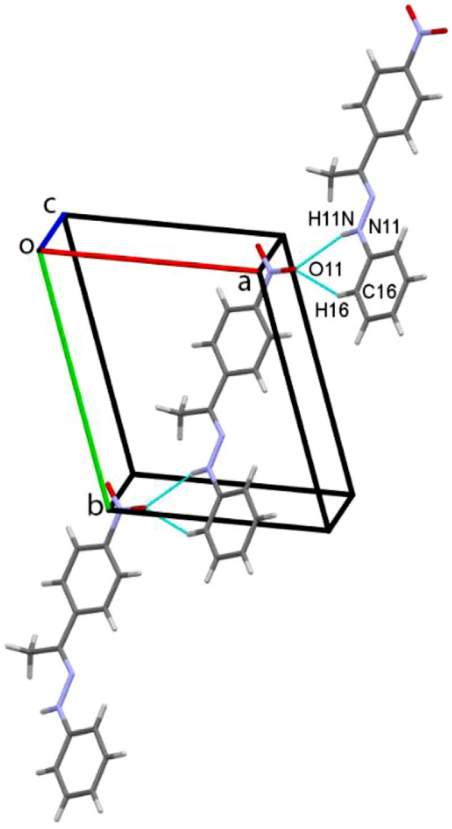

Fig. 4. Chains of M1 molecules of **1c** along the *ab* diagonal.

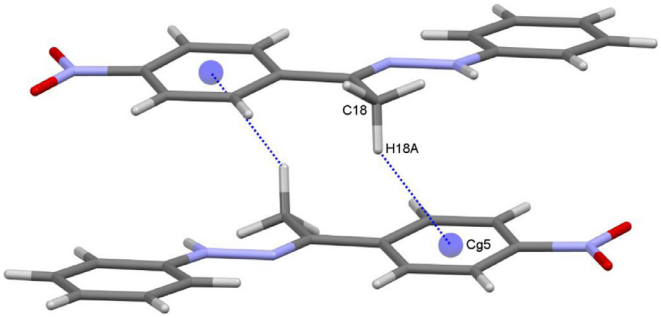

Fig. 5. Inversion dimers of M1 molecules formed by C–H…π contacts.

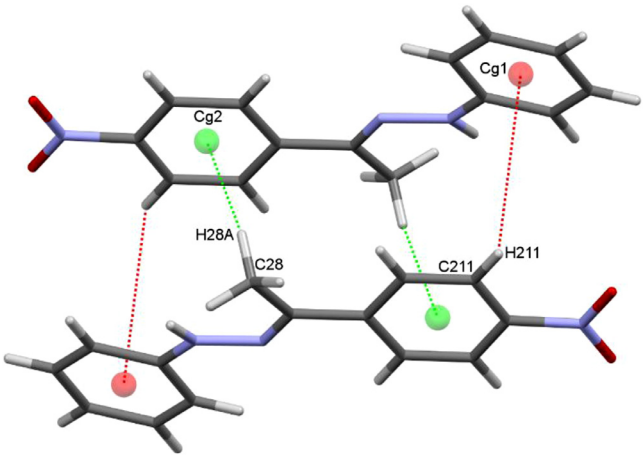

Fig. 6. Inversion dimers of M2 molecules formed by pairs of C–H…π contacts.

bonds while the weaker C–H…π contacts appears as faint red circles. For **2d** the N–H…O hydrogen bond also features strongly with weaker C–H…N and H…H contacts showing less strongly.

Fingerprint plots for **1c** and **2d**, Figs. 13 and 14 show, as expected, that H…H contacts are the most prolific in both cases. A significant feature of the surfaces of both of these compounds is the considerable number of contacts that contribute to the overall surface with the included surface areas of the majority of these being over 1%. For **1c**, the strongest additional contributions come from H…C/C…H and H…O/O…H contacts. Weaker H…N/N…H, C…O, C…N, C…C and O…N interactions are also found, see also Table 4. For **2d**, in addition to the H…H contacts, H…C/C…H, H…O/O…H and H…Br/Br…H contacts predominate with lesser contributions from H…N/N…H, Br…C, Br…Br, C…C and C…N contacts all above 1%; see also Table 4.

Fingerprint plots (Fig. 14) show that H…H contacts are the most prolific with significant contributions also coming from H…C/C…H and H…O/O…H contacts. Weaker H…N/N…H, C…O, C…N, C…C and O…N interactions are also found, see also Table 5.

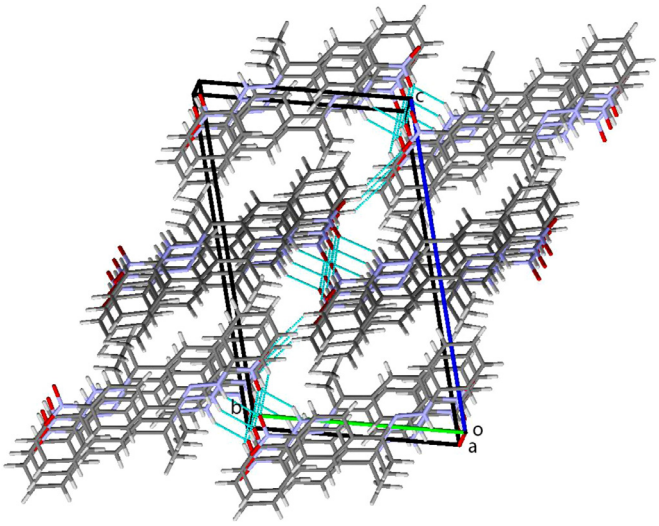

Fig. 7. Overall packing of **1c** viewed along the *a* axis direction.

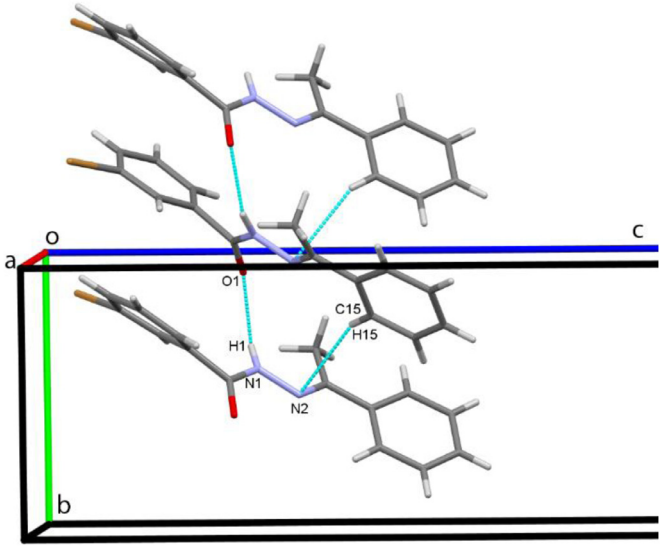

Fig. 8. Chains of molecules of **2d** along the *b* axis.

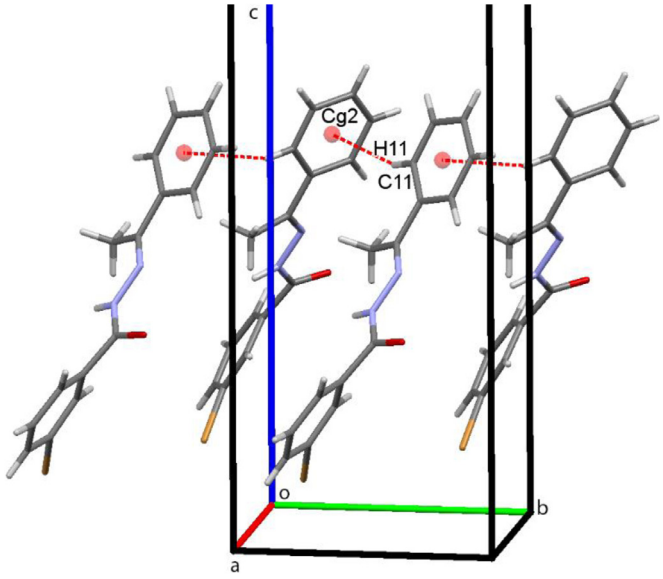

Fig. 9. Chains of molecules of **2d** along the *b* axis generated by C–H…π contacts.

3.4. Theoretical (DFT) studies

3.4.1. HOMO-LUMO analysis

Frontier molecular orbitals (FMO's), the highest occupied molecular orbitals (HOMO) and lowest unoccupied molecular orbitals (LUMO) are important orbitals that determine the stability of molecules. The HOMO acts as an electron donor while the LUMO tends to be an acceptor orbital having the ability to accept electrons. The difference in the HOMO-LUMO energy values characterizes the molecular reactivity, optical polarizability, and kinetic stability of the compound [68]. The HOMO-LUMO energy gaps for compounds **1c** and **2d** are relatively close at 2.36 and 2.38 eV, respectively, demonstrating that **2d** is only slightly more stable and less reactive than **1c**. The shapes of higher occupied MO's are shown in Fig. 15 for both compounds which infer that the HOMO orbitals are delocalized on the hydrazide sections of the molecules. For **1c** the LUMO lies on the substituted aromatic ring, while for **2d** the LUMO involves most of the molecule and the electronic transitions occur from n→π^* and from π→π^*.

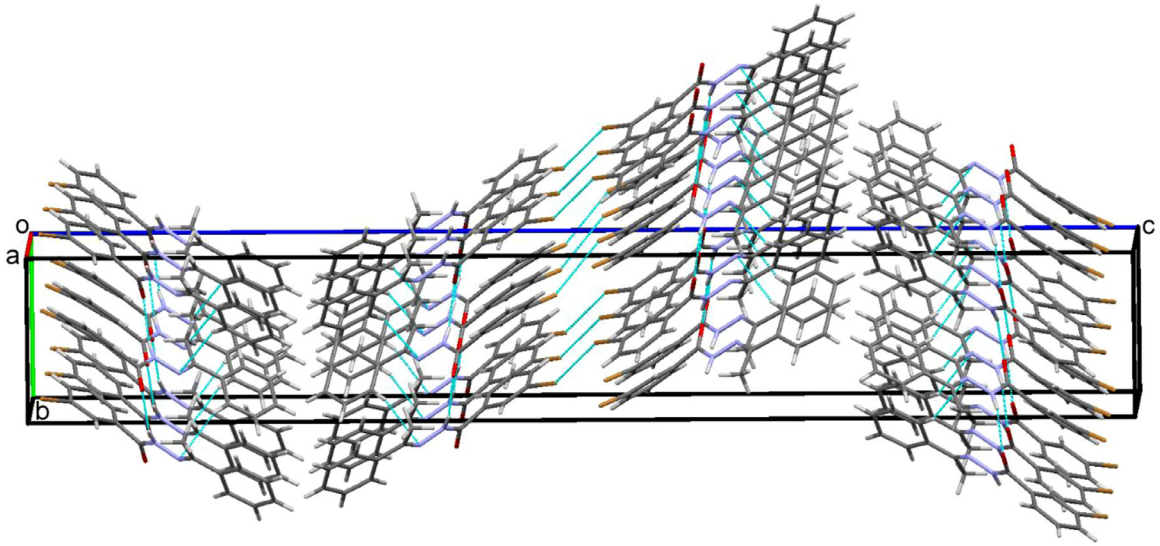

Fig. 10. Overall packing of **2d** viewed along the *a* axis direction.

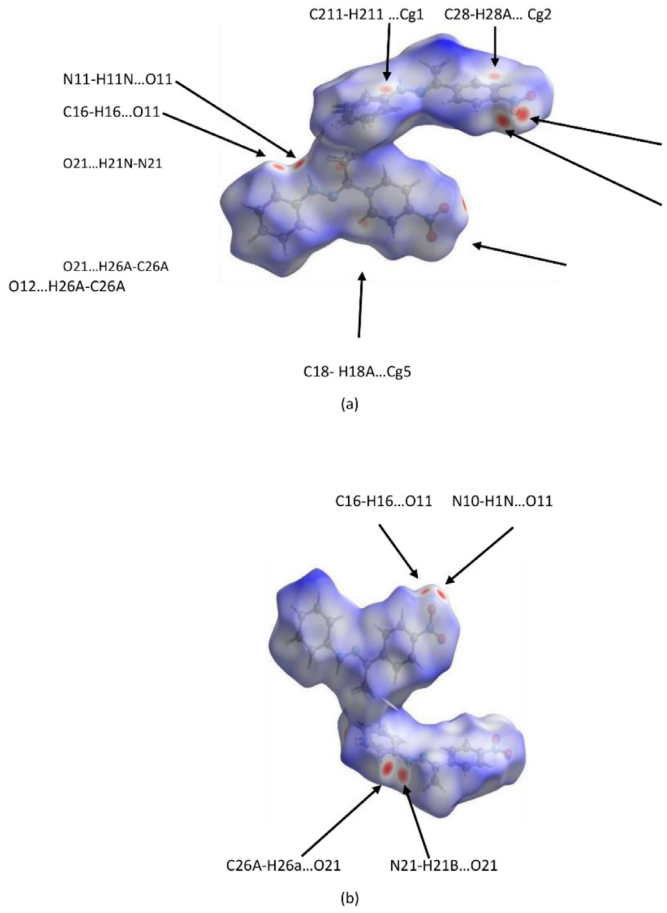

Fig. 11. Hirshfeld surfaces for opposite faces (a) and (b) of the asymmetric unit of **1c**, mapped over d_{norm} in the range –0.2859 to 1.6689 a.u.

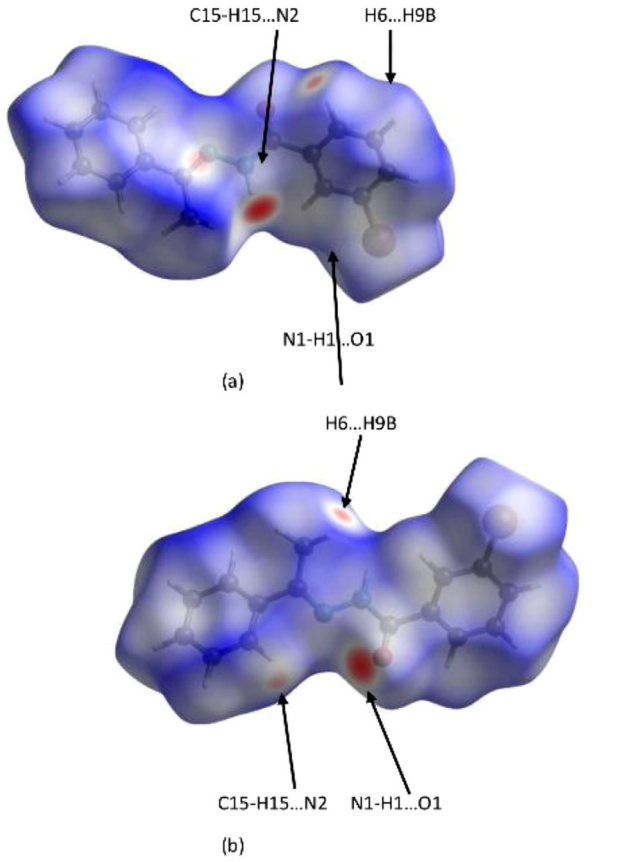

Fig. 12. Hirshfeld surfaces for opposite faces (a) and (b) of the molecule of **2d**, mapped over d_{norm} in the range –0.4184 to 1.3501 a.u.

Table 4
Percentage contributions of interatomic contacts to the Hirshfeld surface for the two molecules that comprise the asymmetric unit of **1c**

Contact	Included surface area (%)
H…H	42.2
H…C/C…H	22.6
H…O/O…H	19.4
H…N/N…H	5.2
C…O	4.3
C…N	3.3
C…C	1.5
O…N	1.3
O…O	0.2
N…N	0.1

Table 5
Percentage contributions of interatomic contacts to the Hirshfeld surface for **2d**

Contacts	Included surface area (%)
H…H	38.0
H…C/C…H	25.0
H…O/O…H	10.7
H…Br/Br…H	10.5
H…N/N…H	4.4
Br…C	3.8
Br…Br	3.0
C…C	2.1
C…N	1.9
N…N	0.5
C…O	0.2

3.4.2. Thermodynamic function analysis

The total energy of a molecule is the sum of the translational, rotational, vibrational, and electronic energies *i.e.*, $E = E_t + E_r + E_v + E_e$. The statistical thermochemical analyses of the title compounds are carried out considering the molecule to be at the standard temperature of 298.15 K and a standard pressure of 1 atm. The thermodynamic properties such as the heat capacity (Cp), enthalpy (H_m), Gibb's free energy (G) and entropy (S^0) were calculated using the DFT/B3LPY program with the 6–311++*G* basis set [69]. Thermodynamic data for the title compounds in the temperature range from 0 to 500 K were calculated using the Moltran software [45] and are given in Fig. 16. From these results, it can be predicted that, with the exception of the Gibb's free energies, the thermodynamics parameter increases with increasing temperature as the vibrational intensities of the title compounds change with temperature [70]. The Gibb's free energies decreases with increase in temperature which shows that the both compounds are stable and do not decompose when temperature is increased in the range investigated. The variation in the thermodynamic parameters with temperature can be seen in Fig. 16. All the thermodynamic data provides helpful information for further study of the compounds. The correlation equations between the thermodynamic properties and temperature satisfy a parabolic formula. The regression coefficients are also determined in the parabolic equations. A partition function is one of the most important thermodynamic parameters that links thermodynamics, spectroscopy and quantum theory and is calculated by the first vibrational level or by the internuclear potential energy values [71]. The partition function can be used to calculate the statistical properties like entropy, free energy, rate constants etc. of a system in thermodynamic equilibrium.

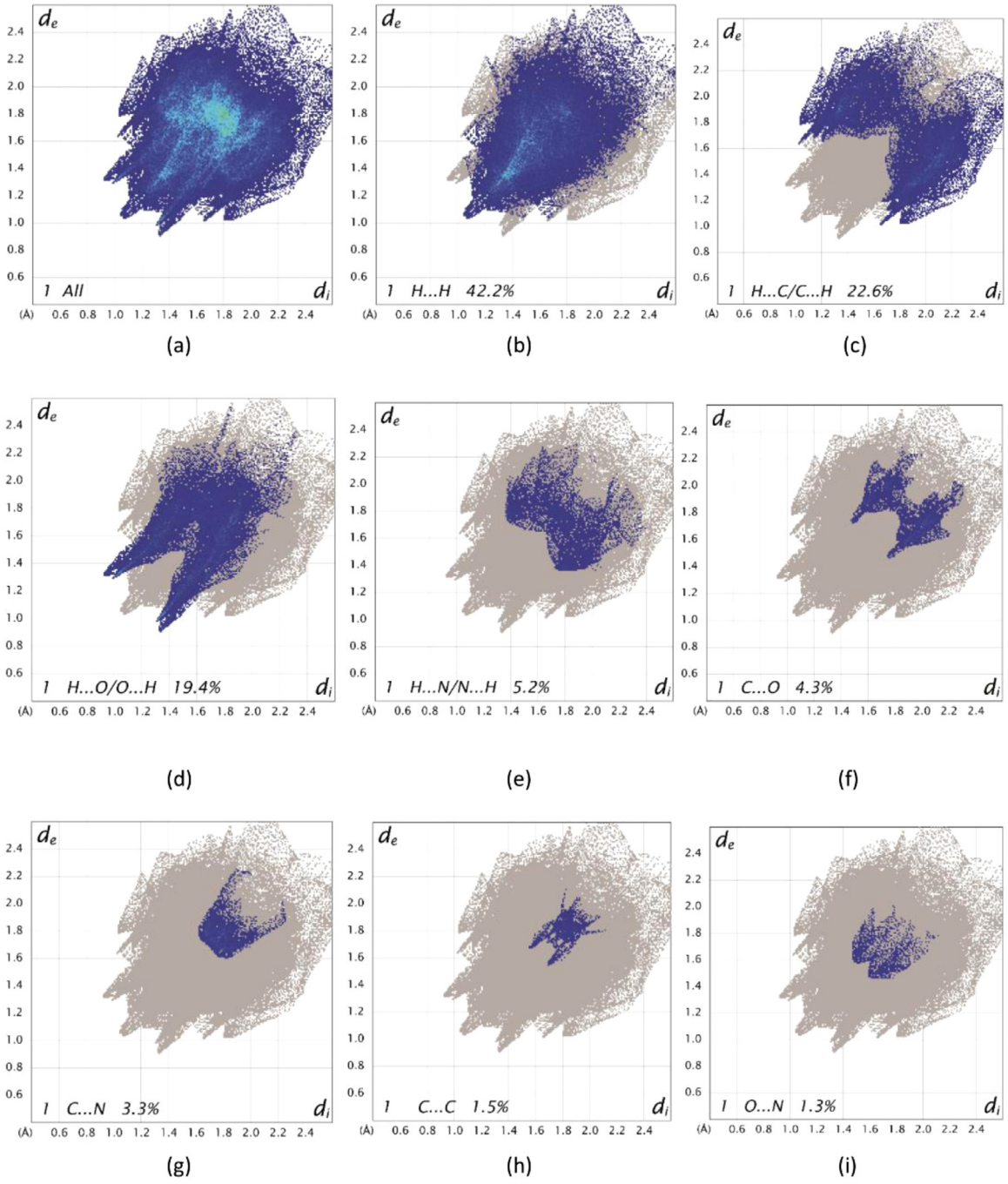

Fig. 13. Two-dimensional fingerprint plots for the asymmetric unit of **1c**, (a), together with (b)-(g) separate contact types and included surface areas for the major individual contacts. Minor contacts contributing less than 1% to the total surface area are not shown here but, for completeness, are shown in Table 4.

3.4.3. Molecular electrostatic potential

The molecular electrostatic potential (MEP) is the visual representation of electronic density for the compounds of interest and is a helpful parameter for the determination of electrophilic and nucleophilic sites and hydrogen binding interactions [72]. MEP maps are also useful for building a relationship of molecular structure with its physicochemical properties [73]. The three-dimensional MEP maps for compounds **1c** and **2d** are presented in Fig. 17 and show the positive and negative sites of these compounds. The color scheme represents the values of electrostatic potential which increases from red to blue. Both MEP maps in Fig. 17 show that the oxygen atoms with red color have negative electrostatic potential and act as a possible site for electrophilic attack (strong repulsion). The most possible regions with blue colours are near the $N-H$ group which make a more reactive site for the nucleophilic attack (strong attraction). Both these sites are also available for hydrogen bonding due to high electronegative atoms *i.e.* nitrogen and oxygen.

3.5. Anticancer activity and computational studies

3.5.1. Drug-likeness

Before bioactivity screening, the compounds were analyzed for their physicochemical properties, including size, shape, lipophilicity, and polar surface area. Descriptors such as the number of rotatable bonds, hydrogen bond donors, hydrogen bond acceptors,

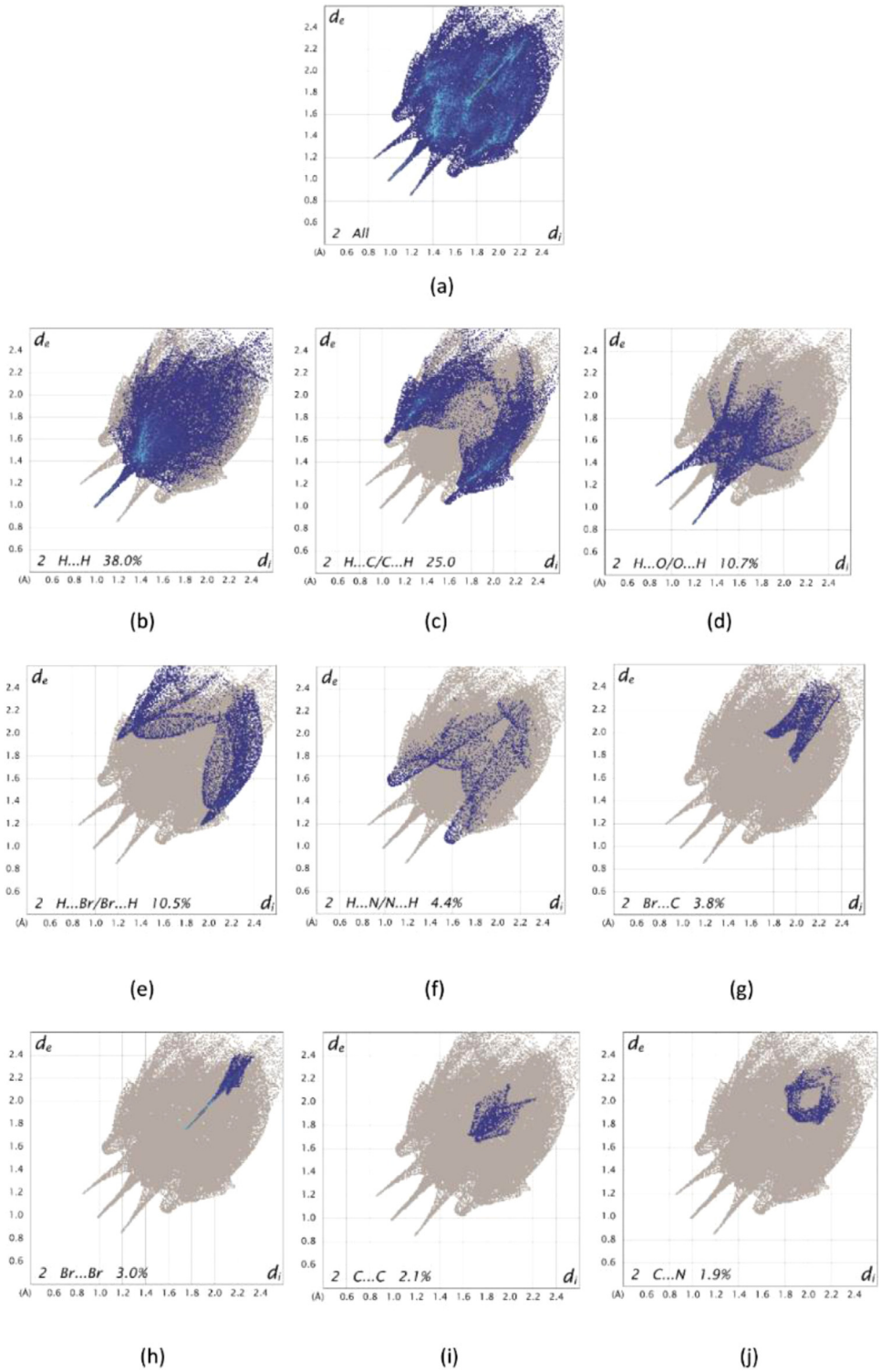

Fig. 14. Two-dimensional fingerprint plots for **2d**, (a), together with (b)-(j) separate contact types and included surface areas for the major individual contacts. Minor contacts contributing less than 1% to the total surface area are not shown here but, for completeness, are shown in Table 5.

Lipinski's acceptors, Lipinski's donors, Lipinski's violations, Lipinski's drug-likeness, log *P* (logarithm of the octanol/water partition coefficient), molecular weight and total polar surface area (TPSA) were computed to access the drug-like properties of the synthesized compounds. *In silico* calculation results revealed that both the synthesized compounds fulfilled the Lipinski's Ro5 [74] and Veber's Ro3 [75] cut-off limits, which suggested that they may have anticancer potential

From the Lipinski Ro5 limit [74], to be considered as drug-like the molecules must have molecular weights $\leq$ 500, log $P \leq 5$, total polar surface area (TPSA) $<$ 140 Å^2, number of hydrogen bond donors (HBD) values ≤ 5 and hydrogen bond acceptor (HBA) values ≤ 10. Veber et al. suggested further modifications to Ro5 [75] with number of rotatable bonds (NOR) of the molecule being $\leq$10 [74]. Molecules that violate more than one of these criteria may have problems with their bioavailability. The detailed results of drug-

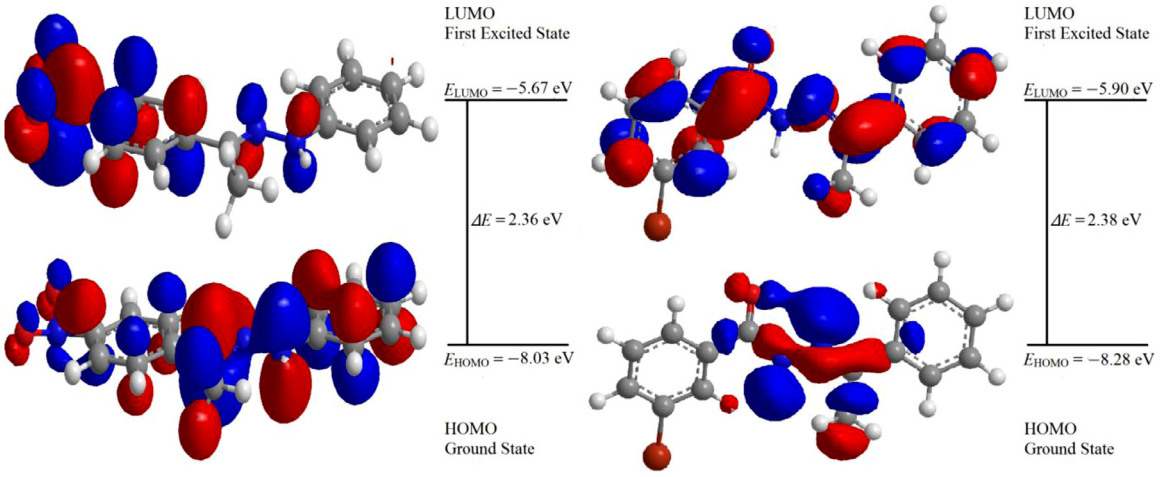

Fig. 15. Frontier molecular orbitals for compounds **1c** (left) and **2d** (right).

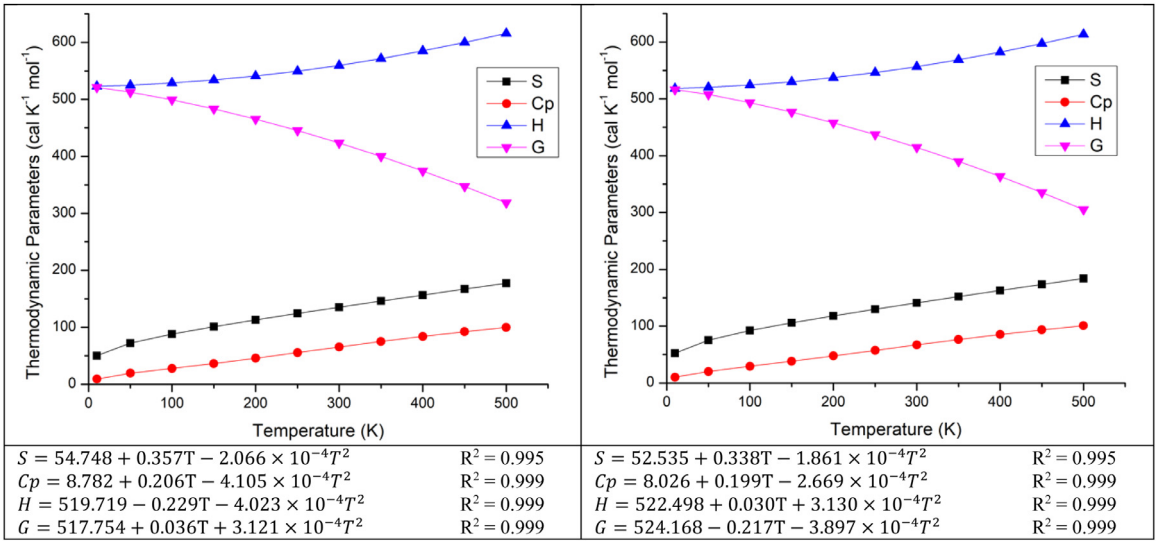

Fig. 16. Variations in thermodynamic parameters with temperature and the correlation equations of **1c** (left) and **2d** (right).

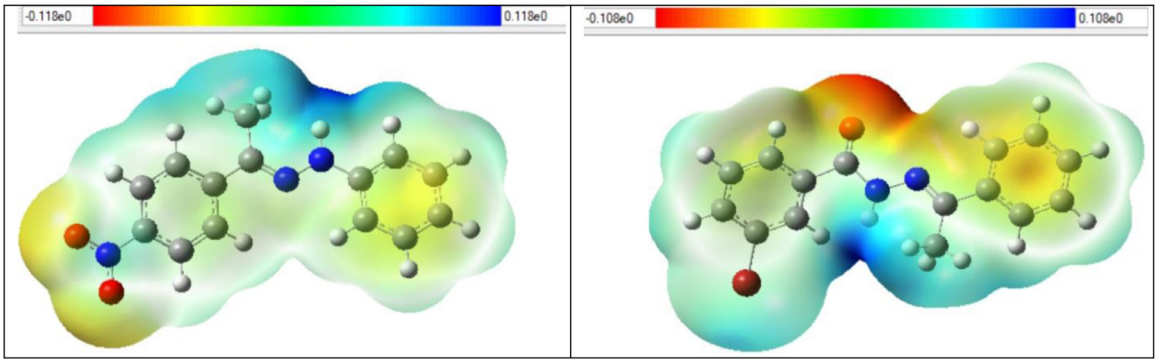

Fig. 17. 3D molecular electrostatic potential map of **1c** (left) and **2d** (right).

likeness of the compounds **1c** and **2d** are tabulated in Table 6 and from these results both compounds are seen fulfill the criteria to be considered as drug-like molecules. Furthermore, the Log P values of compounds **1c** and **2d** indicate good absorption characteristics.

3.5.2. Anticancer activity

The Schiff bases were also tested for their anticancer potential against breast and lung cancer cell lines. In both sexes, lung cancer is the most commonly diagnosed cancer and the leading cause of death closely followed by female breast cancer, prostate cancer and colorectal cancer. Cancer is characterized by an accu-

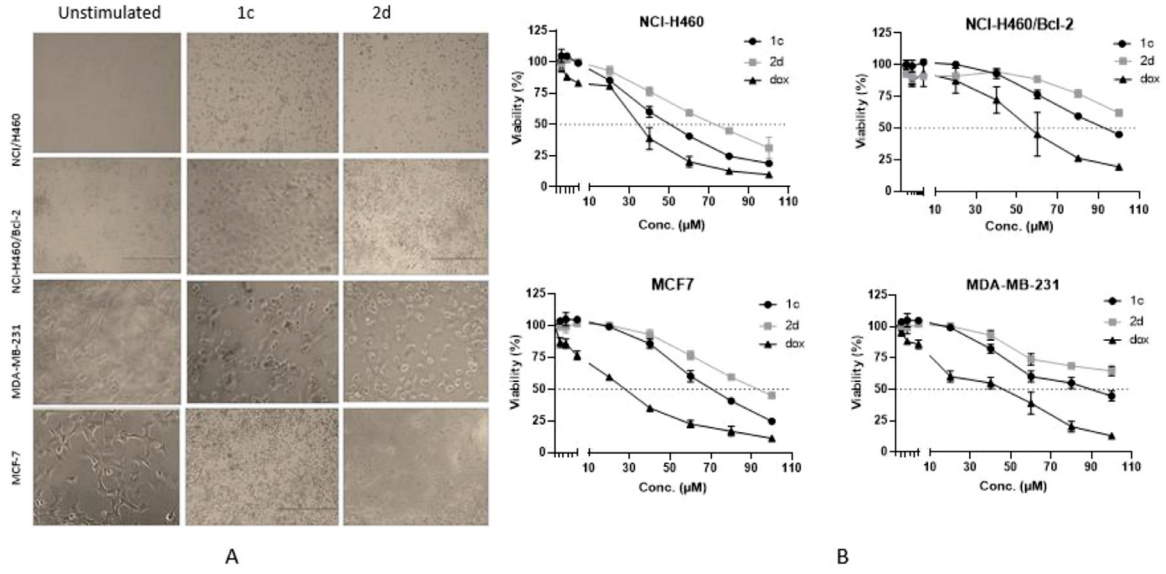

Fig. 18. Cytotoxic effects of Schiff bases on cancer cell lines.

Table 6
Physiochemical properties of compounds **1c** and **2d**

Physicochemical property descriptors	Compound 1c	Compound 2d
Formula	$C_{14}H_{13}N_3O_2$	$C_{15}H_{13}BrN_2O$
Molecular weight	255.27 g/mol	317.18 g/mol
NoR	4	4
HBA	3	2
HBD	1	1
Log P	2.09	2.48
TPSA	70.21 Å²	41.46 Å²

Abbreviations used: NoR = Number of rotatable bonds; **HBA** = Hydrogen bond acceptor; **HBD** = Hydrogen bond donor; **Log P** (Log P (o/w)) = logarithm of the (octanol/water) partition coefficient; **TPSA** = Total polar surface area.

Table 7
IC_{50} (μM) value of compounds against lung and breast cancer cell lines

Cell lines	1c	2d	Doxorubicin
	IC_{50} (μM ± SD)		
NCI-H460	35 ± 5.5	68 ± 4.6	30 ± 4.2
NCI-H460/Bcl-2	90 ± 5.5	N/A	60 ± 5.5
MCF	65 ± 5.4	90 ± 5.5	26 ± 8.5
MDA-MB-231	82 ± 6.5	N/A	42 ± 5.5

N/A where IC_{50} value is above 100 μM.

mulation of genetic variations and the loss of normal cellular regulatory processes. It is a main cause of death worldwide [76,77]. Although chemotherapy is the cornerstone of systemic cancer therapy, it only has a modest effect on overall survival [78]. Thus, there is a great need to develop novel therapeutic modalities to improve survival rates [79].

In this work, the anticancer activity of compounds **1c** and **2d** was evaluated, against lung (NCI-H460, NCI-H460/Bcl-2) and breast cancer (MCF7, MDA-MB-231) cell lines. Cells were stimulated with serial dilutions (0–100 μM) of the compounds and doxorubicin (a positive control) for 24 h. The percentage viability after the 24 h treatment is represented on graphs, Fig. 18, while IC_{50} values are mentioned separately in Table 7.

Fig. 18 reveals that compound **1c** is a more potent inducer of toxicity in all four human cancer cell lines than **2d**, including NCI-H460 and NCI-H460/Bcl-2 (non-small cell lung cancer cell lines), and MDA-MB-231 and MCF-7 (breast cancer cell lines). The lung cancer cell line NCI-H460 was quite sensitive to both compounds, IC_{50} value of **1c** is 35 ± 5.5 μM which is close to that of the standard drug used (30 ± 4.2 μM), whereas its counterpart with overexpression of Bcl-2 showed resistance to compound **1c** and **2d** as well as doxorubicin, which points to the importance of mitochondrial induced toxicity in these cell lines. Breast cancer cells were also resistant to the toxicity induced by **1c** and **2d** at low concentrations as compared to doxorubicin. However, in both cell lines **1c** was a more potent inducer of cell death than **2d** at higher concentrations.

Cytotoxic effects of the two compounds were evaluated in lung and breast cancer cell lines. All cells were seeded in 96 well plates 24 h prior to experiment. Stock solution (1 nM) of the compounds was prepared in DMSO, and cells were stimulated with serial dilutions of both compounds, DMSO was added as a control. 24 h post stimulation A) morphological changes have been observed and images have been captured under microscope. B) Viable cells were stained with crystal violet for 15 min and the absorbance was measured at 550 nm. Values shown are mean ± SD calculated from triplicates. GraphPad Prism 8 software was used to calculate the mean ± SD and IC_{50}.

Epidermal growth factor receptors (EGFR) are frequently overexpressed in breast and non-small cell lung cancer and is a potential therapeutic target for this disease. EGFR is also known as ErbB1 or HER1 and is a member of the receptor family tyrosine kinase (RTK) of cell surface receptors [80]. EGFR regulates differentiation, apoptosis, cell cycle progression, development, and transcription [81]. Overexpression of the EGFR has been observed in a variety of human cancers [82]. EGFR consists of an extracellular domain, a single hydrophobic transmembrane segment, an intracellular portion with a juxtamembrane (JXM) segment, a protein kinase domain, and a carboxyterminal tail [83]. Eps8 is an important active kinase substrate of EGFR that directly binds to the juxtamembrane (JXM) domain of EGFR to form an EGFR/Eps8 complex. The EGFR/ Eps8 complex is involved in regulating cancer progression and might be an ideal target for antitumor therapy [83]. Therefore, to study to putative binding modes, the compounds **1c** and **2d** were analyzed by molecular docking studies to target the EGFR/Eps8 complex in breast and non-small cell lung cancer (NSCLC).

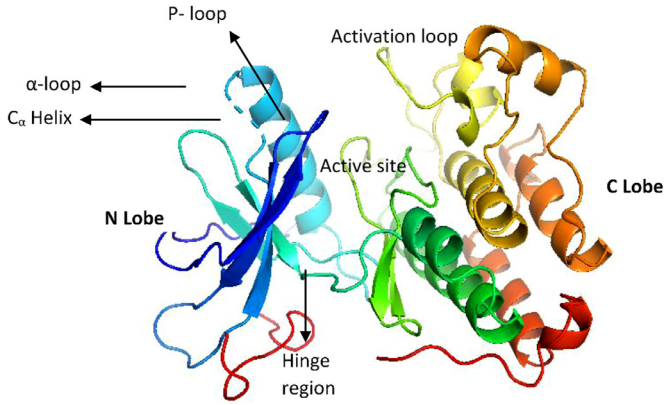

Fig. 19. A cartoon representation of the EGFR protein in a rainbow color pattern. Some important regions of EGFR such as active site, hinge region, p-loop, activation loop, α-loop, *C*-lobe and *N*-lobe are labelled.

3.5.3. Molecular docking studies

Computational approaches were employed to investigate the possible basis for preferential binding of ligands to the active conformation of EGFR-TKD.

3.5.3.1. EGFR structure. EGFR, a transmembrane glycoprotein is composed of 1186 residues, including three parts: extracellular receptor region, transmembrane structure, and intracellular tyrosine kinase region [80]. The structure and function of the intracellular domain of EGFR (from Gly696 to Ile1018) has been a major topic of research. There are seven α-helices and seven β-sheets in the intracellular domain, and the inhibitor can be firmly locked in the 'mouth-like' structure (Fig. 19) and compete with the natural substrate for the ATP binding site. Fig. 19 shows that the groove in the 'mouth' consists of five functional regions, which are the P-loop (Ser720 to Gly724), the α-loop (Arg748 to Ser752), a hinge-region (Gln791 to Leu798), a DFG motif (Thr854 to Arg858) and a Cα-helix (Pro753 to Ser768).

The difference between inhibitory activities of analogues (**1c** and **2d**) studied in this work led us to make structural comparisons in terms of their intermolecular interactions that may mediate protein-ligand binding, their relative location in the active site, their size, shape, and physicochemical properties. In order to investigate the binding mode of the inhibitors and their interaction with amino acid residues of EGFR (PDB ID: 2GS6), a molecular docking study of the two synthesized compounds was performed. The docked conformations further assisted in the identification of the relative location of the co-crystallized inhibitors and the reference molecules in the protein architecture of EGFR. Doxorubicin was used as a reference drug in biological screening; therefore, it was also docked with the enzyme to compare its binding interaction.

3.5.3.2. Molecular docking and binding analysis. For elucidation of the molecular basis of the mechanism of inhibition, the compounds were docked computationally to the active site of EGFR. In this study, first the protein structure (2GS6: 2.0 Å) was retrieved from Protein Data Bank (PDB). The protein was already bound with ligands in its crystal structure. The bound co-crystallized ligands were removed from the active pocket of the protein to study the inhibition mechanism of the active compounds. All the ligands were docked in 20 different conformations with variable energy values. All the preferred docked conformations formed one cluster inside the pockets as shown in Fig. 20.

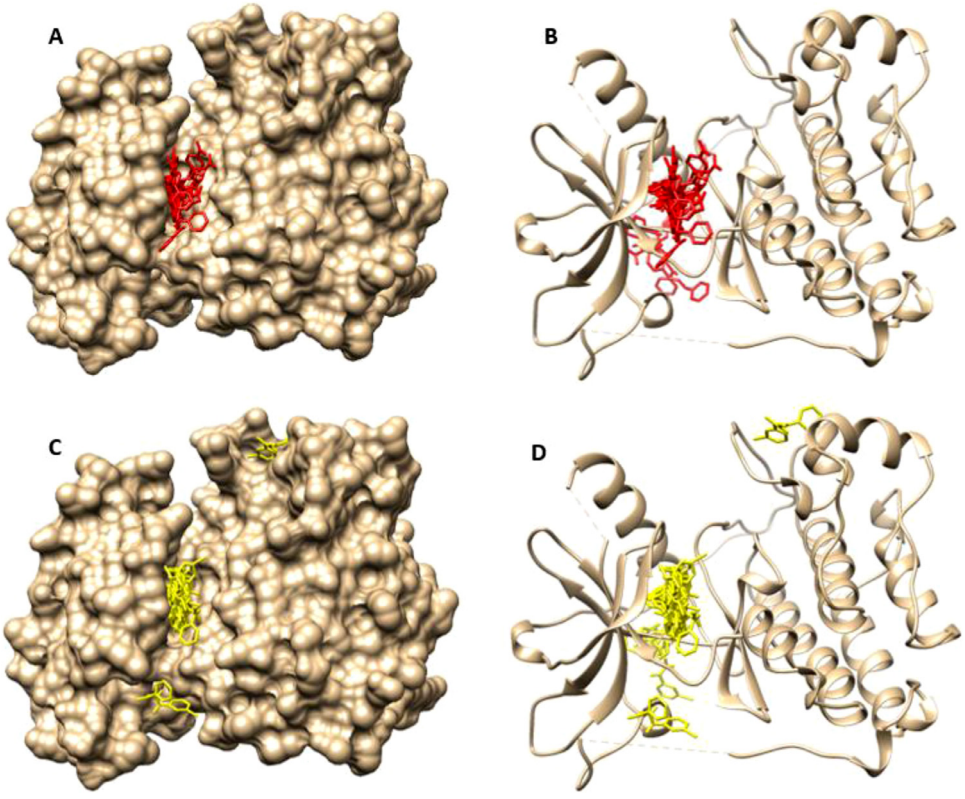

Fig. 20. Superimposition of the twenty different docked conformations of the inhibitors in the active site of EGFR (PDB: 2GS6); **1c** is shown in red (A and B) forming two clusters whereas **2d** is shown in yellow (C and D), forming three clusters inside the pockets of the enzyme EGFR; a closer view. Receptor is shown in beige in surface A and C and in ribbon form in B and D while the ligands are shown in sticks form. (For interpretation of the references to colour in this figure legend, the reader is referred to the web version of this article.)

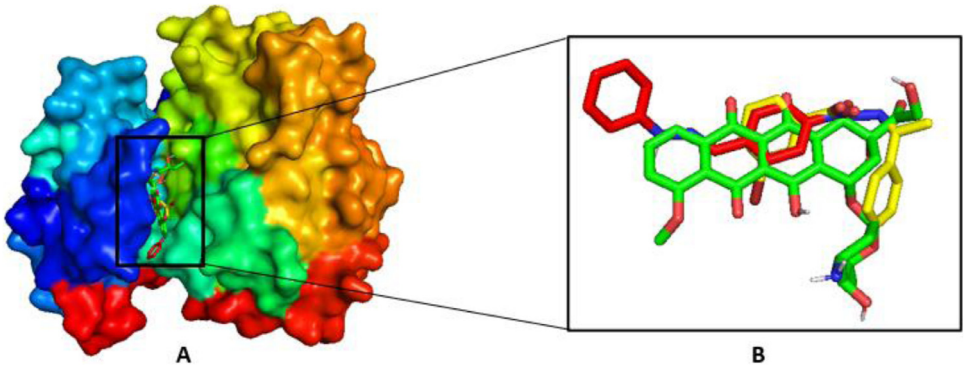

Fig. 21. A) An overlay of the docked orientations of the preferred conformations of compounds **1c** and **2d** and doxorubicin in the active pocket of EGFR (surface view-rainbow color). B) Minimal energy conformations and relative positioning of all 3 variants. (For interpretation of the references to colour in this figure legend, the reader is referred to the web version of this article.)

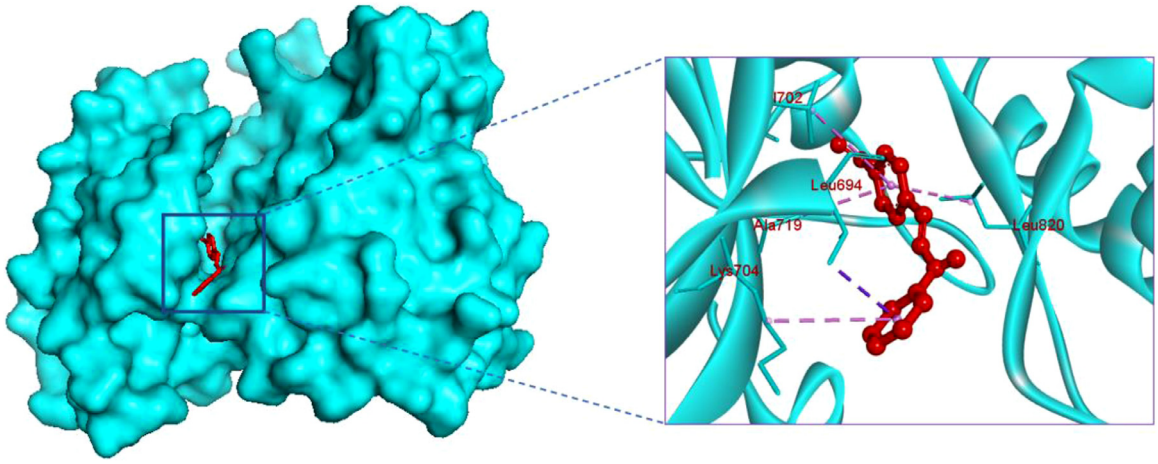

Fig. 22. Docking pose of compound **1c** in 3D space; receptor is shown in cyan surface (left) and in ribbons (right). Ligand **1c** is shown in red ball and stick model. Receptor is shown in cyan colored ribbons while the key residues are shown in stick mode. Interacting residues are labeled in maroon. (For interpretation of the references to colour in this figure legend, the reader is referred to the web version of this article.)

All the docked conformations for each compound were analyzed and it was found that the most favorable docked poses with maximum number of interactions were those, which were ranked the highest, based on the least binding energy. The binding energy was calculated as a negative value by the software. From the molecular docking calculation results, we chose variants with the minimal energy of the enzyme–inhibitor complex. The most favorable docking poses of the 20 docked conformations for each compound were retained to investigate the interactions of the docked conformations within the active site. The detailed docking results are also discussed. It has been observed from conformational analysis and relative positioning that the compounds **1c** and **2d** are positioned in the active pocket in the same way as doxorubicin (Fig. 21).

It has been observed that compound **1c** occupies the hydrophobic pocket of the binding site and makes hydrophobic interactions in the active site of EGFR (Fig. 22). Both the phenyl rings are positioned in a hydrophobic pocket formed by the side chains of Leu694, Ala719, Val702 and Leu820. Most of the amino acid residues form pi-alkyl interactions with aryl rings of compound **1c** (Fig. 22).

In compound **2d**, the phenyl ring is adjacent to the carbonyl moiety predominantly pi-alkyl hydrophobic interactions occur with Ala719 and Leu820 (Fig. 23). However, the phenyl ring adjacent to $C = N$ linkage also forms pi-cation interactions with Lys721 at a distance of 3.44 Å. Another important interaction of hydrazide **2d** with the receptor is a hydrogen bond between O–H of Thr766 and the carbonyl O of compound **2d** In contrast doxorubicin forms two hydrogen bonds with Thr766 and Thr830. It has also been observed that the relative positioning of the two molecules (**2d** and doxorubicin) is slightly different (Fig. 23). Compound **2d** preferentially occupies the space near the p-loop region while doxorubicin prefers to reside between the p-loop and α-loop region. These results clearly conclude that good activities of these inhibitors are attributed to quite low binding energy, effective positioning of the compounds in the active site near activation loop and multiple interactions with the key residues inside the active site of the target structure.

3.5.4. Pharmacokinetics

The ADMET properties of the Schiff bases (**1c** and **2d**) were calculated using SwissADME (Table 8). It was found that both the compounds could be absorbed by the human intestine. Nevertheless, the compounds were predicted as non-substrates for P-glycoprotein (P-gp) which effluxes drugs and various compounds to undergo further metabolism and clearance. Many of the human microsomal cytochrome P450s catalyze the metabolism of a wide variety of compounds including xenobiotics and drugs. Drug metabolism *via* the cytochrome P450 system has emerged as an important determinant in the occurrence of several drug interactions that can result in reduced pharmacological effects and adverse drug reactions [84]. Most drugs can exhibit decreased efficacy due to rapid metabolism, but drugs with active metabolites can display increased drug effect and/or toxicity due to enzyme in-

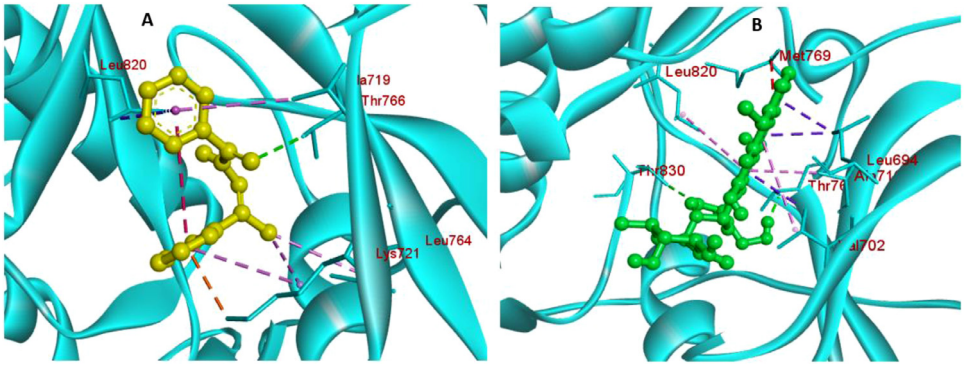

Fig. 23. Docking pose of ligands in 3D space; receptor is shown in ribbons and ligands are shown in ball and stick model. A) Compound **2d** is shown as yellow sticks; B) Reference compound doxorubicin is shown as green sticks; Receptor is shown in cyan colored ribbons while the key residues are shown in stick mode. Interacting residues are labeled in maroon. Pink dotted lines indicate pi-pi interactions, orange dotted lines indicate pi-cation interactions while green dotted lines indicate hydrogen bond interactions. (For interpretation of the references to colour in this figure legend, the reader is referred to the web version of this article.)

Table 8
Pharmacokinetic properties of compounds **1c** and **2d**

Pharmacokinetic property descriptor	Compound 1c	Compound 2d
GI absorption	High	High
BBB permeant	Yes	Yes
P-gp substrate	No	No
CYP1A2 inhibitor	Yes	Yes
CYP2C19 inhibitor	Yes	Yes
CYP2C9 inhibitor	Yes	Yes
CYP2d6 inhibitor	No	No
CYP3A4 inhibitor	No	No

duction [84]. Both the Schiff bases were predicted to have potential against inhibition of CYP2C9, CYP2C19, and CYPA12 (Table 8). However, none of the imines are predicted to have potential to be the inhibitor of CYP2d6 as shown in Table 8.

4. Conclusions

In summary, the present study reports the synthesis of two Schiff bases (*E*)−1-(1-(4-nitrophenyl)ethylidene)−2-phenylhydrazine **1c** and (*E*)−3–bromo-*N*'-(1-phenylethylidene)benzohydrazide **2d.** The structures of both compounds were fully established by spectroscopic and X-ray crystallographic methods. Non-covalent interactions governing the overall topology of the supramolecular architectures in both compounds were investigated using X-ray crystallography and computational methods. The conspicuous role of hydrogen bonding, $\pi\ldots\pi$ stacking, C–H…π and Br…Br interactions was further rationalized using Hirshfeld surface analysis. Bioevaluation against four cancer cell lines revealed that compound **1c** was more potent inducer of toxicity in all the tested human cancerous cell lines, i.e.; NCI-H460 and NCI-H460/Bcl-2 (non-small cell lung cancer cell lines), MDA-MB-231 and MCF-7 (breast cancer cell lines) compared to **2d.** The binding modes of both Schiff bases were rationalized using molecular docking studies. Furthermore, the compounds also showed favorable pharmacokinetic properties.

Declaration of Competing Interest

The authors declare that they have no known competing financial interests or personal relationships that could have appeared to influence the work reported in this paper.

Acknowledgements

H.A. and L.D. are grateful to the Higher Education Commission of Pakistan for financial support under SRGP program. J.S. thanks the Chemistry Department, University of Otago for support of his work. L.D. is thankful to Peter Scheurich Lab at institute of cell biology and immunology, university of Stuttgart, Germany for providing human cancerous cell lines NCI-H460 and NCI-H460/Bcl-2 (non-small cell lung cancer), MDA-MB-231 and MCF-7 (breast cancer).

Supplementary materials

Supplementary material associated with this article can be found, in the online version, at doi:10.1016/j.molstruc.2021.130223.

References

[1] L.A. Estroff, A.D. Hamilton, Chem. Rev. 104 (2004) 1201–1217.
[2] J.T. Lenthall., J.A. Foster., K.M. Anderson., M.R. Probert., J.A.K. Howard, J.W. Steed, Cryst. Eng. Comm. 13 (2011) 3202–3212.
[3] R. Custelcean, Chem. Commun. (2008) 295–307.
[4] C. Caltagirone, G.W. Bates, P.A. Gale, M.E. Light, Chem. Commun. (2008) 61–63.
[5] J.W. Steed, Chem. Commun. 47 (2011) 1379–1383.
[6] (a) J.W. Steed, J.L. Atwood, Supramol. Chem. (2009); (b) A. Bauzá, S.K. Seth, A. Frontera, Coord. *Chem. Rev.* 384 (2019) 107–125.
[7] C.A. Hunter, Chem. Soc. Rev. 23 (1994) 101–109.
[8] (a) T. Shimizu, M. Masuda, H. Minamikawa, Chem. Rev. 105 (2005) 1401–1444; (b) E.R. Kay, D.A. Leigh, F. Zerbetto, Angew. Chem., Int. Ed. 46 (2007) 72–191; (c) J.D. Fox, S.J. Rowan, Macromolecules 42 (2009) 6823–6835.
[9] G.R. Desiraju, Chem. Commun. (2005) 2995–3001.
[10] G.R. Desiraju, Acc. Chem. Res. 35 (2002) 565–573.
[11] S.S. Kuduva, D.C. Craig, A. Nangia, G.R. Desiraju, J. Am. Chem. Soc. 121 (1999) 1936–1944.
[12] G.R. Desiraju, T. Steiner, The Weak Hydrogen Bond in Structural Chemistry and Biology, Oxford University Press, Oxford, U.K., 1999.
[13] T. Steiner, Chem. Commun. (1997) 727–734.
[14] C.R. Kaiser, K.C. Pais, M.V.N. de Souza, J.L. Wardell, S.M.S.V. Wardell, E.R.T. Tiekink, Cryst. Eng. Comm. 11 (2009) 1133–1140.
[15] (a) L.-F. Ma, L.-Y. Wang, J.-L. Hu, Y.-Y. Wang, S.R. Batten, J.-G. Wang, Cryst. Eng. Comm. 11 (2009) 777–783; (b) R. Bag, Y. Sikdar, S. Sahu, D.K. Maiti, A. Frontera, A. Bauzá, M.G.B. Drew, S. Goswani, Dalton Trans. 47 (2018) 17077–17085; (c) B. Naskar, A. Bauzá, A. Frontera, D.K. Maiti, C.D. Mukhopadhyay, S. Goswami, Dalton Trans. 47 (2018) 15907–15916; (d) K. Ghosh, K. Harms, A. Bauzá, A. Frontera, S. Chattopadhyay, Cryst. Eng. Comm 20 (2018) 7281–7292; (e) S. Saha, N. Biswas, A. Sasmal, C.J. Gómez-García, E. Garribba, A. Bauza, A. Frontera, G. Pilet, G.M. Rosair, S. Mitra, C.R. Choudhury, Dalton Trans 47 (2018) 16102–16118.
[16] (a) H. Zhou, L. Chen, R. Chen, Z.-H. Peng, Y. Song, Z.-Q. Pan, Q.-M. Huang, X.-L. Hu, Z.-W. Bai, Cryst. Eng. Comm. 11 (2009) 671–679; (b) S. Dutta, S. Jana, P. Mahapatra, A. Bauzá, A. Frontera, A. Ghosh, Cryst. Eng. Comm. 20 (2018) 6490–6501; (c) A. Castiñeiras, I. García-Santos, J.M. González-Pérez, A. Bauzá, J.K. Zaręba, J. Niclós-Gutiérrez, R. Torres, E. Vílchez, A. Frontera, Cryst. Growth Des. 18 (2018) 6786–6800; (d) M.N. Piña, P. Rodríguez, M.S. Gutiérrez, D. Quiñonero, J. Morey, A. Frontera, Chem. Eur. J. 24 (2018) 12820–12826; (e) T. Maity, H. Mandal, A. Bauza, B.C. Samanta, A. Frontera, S.K. Seth, New J. Chem. 42 (2018) 10202–10213; (f) G. Mahmoudi, S.K. Seth, A. Bauza,

F.I. Zubkov, A.V. Gurbanov, J. White, V. Stilinovic, T. Doert, A. Frontera, Cryst. Eng. Comm 20 (2018) 2812–2821.
[17] Y.R. Zhong, M.L. Cao, H.J. Mo, B.H. Ye, Cryst. Growth Des. 8 (2008) 2282–2290.
[18] A. Gogoi, S.M. Nashre-ul-Islam, A. Frontera, M.K. Bhattacharyya, Inorg. Chim. Acta. 484 (2019) 133–141.
[19] (a) S. Takahashi, T. Jukurogi, T. Katagiri, K. Uneyama, Cryst. Eng. Comm 8 (2006) 320–326; (b) R. Barbas, R. Prohens, A. Bauzá, A. Franconetti, A. Frontera, Chem. Commun. 55 (2019) 115–118; (c) G. Mahmoudi, A.A. Khandar, F.A. Afkhami, B. Miroslaw, A.V. Gurbanov, F.I. Zubkov, A. Kennedy, A. Franconetti, A. Frontera, Cryst. Eng. Comm 21 (2019) 108–117; (d) B. Ramezanpour, M. Mirzaei, V. Jodaian, M.N. Shahrak, A. Frontera, E. Molins, Inorg. Chim. Acta. 484 (2019) 264–275.
[20] (a) A.N. Sokolov, T. Friscic, S. Blais, J.A. Ripmeester, L.R. MacGillivray, Cryst. Growth Des. 6 (2006) 2427–2428; (b) S.M. Nashre-ul-Islam, D. Dutta, A. Frontera, M.K. Bhattacharyya, Inorg. Chim. Acta. 487 (2019) 424–432; (c) D. Quiñonero, A. Frontera, Inorganics 7 (2019) 1–20 9; (d) M. Kumar, H.N. Sheikh, A. Franconetti, J.K. Zaręba, A. Frontera, New J. Chem. 43 (2019) 2179–2195; (e) S.K. Panigrahi, J. *Amino Acids.* 34 (2008) 617–633.
[21] G. Toth, S.G. Bowers, A.P. Truong, G. Probst, Curr. Pharm. Des. 13 (2007) 3476–3493.
[22] S. Sarkhel, G.R. Desiraju, Proteins: Struct., Funct., Genet 54 (2004) 247–259.
[23] E. Arbely, I.T. Arkin, J. Am. Chem. Soc. 126 (2004) 5362–5363.
[24] B.K. Ho, P.M. Curmi, J. Mol. Biol. 317 (2002) 291–308.
[25] O.B. Berryman, V.S. Bryantsev, D.P. Stay, D.W. Johnson, B.P. Hay, J. Am. Chem. Soc. 129 (2007) 48–58.
[26] (a) Y. Bai, B.-.G. Zhang, C.-.Y. Duan, D.-.B. Dang, Q.-.J. Meng, New J. Chem. 30 (2006) 266–271; (b) S. Khan, S. Roy, K. Harms, A. Bauzá, A. Frontera, S. Chattopadhyay, Inorg. Chim. Acta. 487 (2019) 465–472.
[27] K.-.J. Chang, D. Moon, M.S. Lah, K.-.S. Jeong, Angew. Chem., Int. Ed. 44 (2005) 7926–7929.
[28] (a) T. Hajiashrafi, R. Zekriazadeh, K.J. Flanagan, F. Kia, A. Bauzá, A. Frontera, M.O. Senge, Acta Cryst C75 (2019) 178–188; (b) U. Saha, D. Dutta, H. Nath, A. Franconetti, A. Frontera, M.K. Bhattacharyya, Inorg. Chim. Acta. 488 (2019) 159–169; (c) F.A. Afkhami, G. Mahmoudi, A.A. Khandar, A. Franconetti, E. Zangrando, N. Qureshi, J. Lipkowski, A.V. Gurbanov, A. Frontera, Eur. J. Inorg. Chem. (2019) 262–270; (d) H. Ihm, S. Yun, H.G. Kim, J.K. Kim, K.S. Kim, Org. Lett. 4 (2002) 2897–2900.
[29] J.S. González-González, F.J. Martínez-Martínez, A.L.P. Campos, M. de Jesus Rosales-Hoz, E.V. García-Báez, I.I. Padilla-Martínez, CrystEngComm 13 (2011) 4748–4761.
[30] (a) R. Carrillo, M. López-Rodríguez, V.S. Martin, T. Martín, Angew. Chem., Int. Ed. 48 (2009) 7803–7808; (b) Y. Kobayashi, T. Kurasawa, K. Kinbara, K. Saigo, J. Org. Chem. 69 (2004) 7436–7441; (c) Y. Ryan, P.W. Peterson, C.M. Hadad, J.D. Badjic, Chem. Commun. 50 (2014) 9086–9089; (d) P. Sozzani, A. Comotti, S. Braco, R. Simonutti, Chem. Commun. (2004) 768; (e) H. Brunner, T. Tsuno, M. Bodensteiner, Organometallics 33 (2014) 2257–2265; (f) E.C. Constable, K. Harris, C.E. Housecroft, M. Neuburger, J.A. Zampese, Cryst. Eng. Comm 12 (2010) 2949–2961.
[31] (a) I. Khan, A. Ibrar, J. Simpson, CrystEngComm 16 (2014) 164–174; (b) I. Khan, P. Panini, S.U.-D. Khan, U.A. Rana, H. Andleeb, D. Chopra, S. Hameed, J. Simpson, Cryst. Growth Des. 16 (2016) 1371–1386; (c) R. Shukla, I. Khan, A. Ibrar, J. Simpson, D. Chopra, CrystEngComm 19 (2017) 3485–3498; (d) M. Kazmi, A. Ibrar, H.S. Ali, M. Ghufran, A. Wadood, U. Flörke, J. Simpson, A. Saeed, A. Frontera, I. Khan, J. Mol. Struct. 1197 (2019) 458–470; (e) A. Bibi, I. Khan, H. Andleeb, J. Simpson, M.N. Tahir, S. Hameed, A. Frontera, J. Mol. struct. 1227 (2021) 129425.
[32] Y. Toledano-Magaña, J.C. García-Ramos, M. Navarro-Olivarria, M. Flores-Alamo, M. Manzanera-Estrada, L. Ortiz-Frade, B.M. Cabrera-Vivas, Molecules 20 (6) (2015) 9929–9948.
[33] (a) H. Andleeb, I. Khan, A. Franconetti, M.N. Tahir, J. Simpson, S. Hameed, A. Frontera, Cryst. Eng. Comm 21 (11) (2019) 1780–1793; (b) C.-.H. Kao, T.-.K. Tao, C.-.H. Kao, P.P.T. Sah, J. Chin. Chem. Soc. (Peking) 4 (1936) 69–74.
[34] Bruker*APEX2* and *SAINT*, Bruker AXS Inc., Madison, Wisconsin, USA, 2007.
[35] BrukerSADABS, Bruker AXS Inc., Madison, Wisconsin, USA, 2005.
[36] G.M. Sheldrick, Acta Cryst A64 (2008) 112–122.
[37] G.M. Sheldrick, Acta Cryst C71 (2015) 3–8.
[38] K.A. Hunter, J. Simpson, TITAN2000, University of Otago, New Zealand, 1999.
[39] C.F. Macrae, I.J. Bruno, J.A. Chisholm, P.R. Edgington, P. McCabe, E. Pidcock, L. Rodriguez-Monge, R. Taylor, J. van de Streek, P.A. Wood, J. Appl. Cryst. 41 (2008) 466–470.
[40] A.L. Spek, Acta Cryst D65 (2009) 148–155.
[41] L.J. Farrugia, J. Appl. Cryst. 32 (1999) 837–838.
[42] N.K. Chithra, C. James, Vib. Spectrosc. 59 (2012) 9–17.
[43] M.J. Frisch, G.W. Trucks., H.B. Schlegel, G.E. Scuseria, M.A. Robb, J.R. Cheeseman, G. Scalmani, V. Barone, B. Mennucci, G.A. Petersson, H. Nakatsuji, M. Caricato, X. Li, H.P. Hratchian, A.F. Izmaylov, J. Bloino, G. Zheng, J.L. Sonnenberg, M. Hada, M. Ehara, K. Toyota, R. Fukuda, J. Hasegawa, M. Ishida, T. Nakajima, Y. Honda, O. Kitao, H. Nakai, T. Vreven, J.A. Montgomery Jr., J.E. Peralta, F. Ogliaro, M. Bearpark, J.J. Heyd, E. Brothers, K.N. Kudin, V.N. Staroverov, R. Kobayashi, J. Normand, K. Raghavachari, A. Rendell, J.C. Burant, S.S. Iyengar, J. Tomasi, M. Cossi, N. Rega, J.M. Millam, M. Klene, J.E. Knox, J.B. Cross, V. Bakken, C. Adamo, J. Jaramillo, R. Gomperts, R.E. Stratmann, O. Yazyev, A.J. Austin, R. Cammi, C. Pomelli, J.W. Ochterski, R.L. Martin, K. Morokuma, V.G. Zakrzewski, G.A. Voth, P. Salvador, J.J. Dannenberg, S. Dapprich, A.D. Daniels, Ö. Farkas, J.B. Foresman, J.V. Ortiz, J. Cioslowski, D.J. Fox, Gaussian 09, Gaussian, Inc., Wallingford CT, 2009.
[44] S. Grimme, J. Antony, S. Ehrlich, H.A. Krieg, J. Chem. Phys. 132 (2010) 154104.
[45] M. Karabacak, E. Kose, A. Atac, E.B. Sas, A.M. Asiri, M. Kurt, *J. Mol. Struc*t. 1076 (2014) 358–372.
[46] E.R. Johnson, S. Keinan, P. Mori-Sańchez, J. Contreras-Garciá, A.J. Cohen, W. Yang, J. Am. Chem. Soc. 132 (2010) 6498–6506.
[47] T. Lu, F. Chen, J. Comput. Chem. 33 (2012) 580–592.
[48] W. Humphrey, A. Dalke, K. Schulten, J. Mol. Graph. 14 (1996) 33–38.
[49] O. Trott, A.J. Olson, J. Comput. Chem. 31 (2010) 455–461.
[50] M.F. Sanner, J. Mol. Graph. Mod. 17 (1999) 57–61.
[51] N.M. O'Boyle, M. Banck, C.A. James, C. Morley, T. Vandermeersch, G.R. Hutchison, J. Cheminform. 3 (2011) 1–14 33.
[52] The PyMOL Molecular Graphics System, Version 1.2r3pre, Schrödinger, LLC.
[53] E.F. Pettersen, T.D. Goddard, C.C. Huang, G.S. Couch, D.M. Greenblatt, E.C. Meng, T.E. Ferrin, J. Comput. Chem. 25 (2004) 1605–1612.
[54] A. Daina, O. Michielin, V. Zoete, Sci. Rep., 7 (2017) 42717 1-13.
[55] H. Andleeb, M. Hussain, S.A. Ejaz, J. Sevigny, M. Farman, M. Yasinzai, J. Zhang, J. Iqbal, S. Hameed, Bioorg. Chem. 101 (2020) 103999.
[56] C.R. Groom, I.J. Bruno, M.P. Lightfoot, S.C. Ward, Acta Cryst B72 (2016) 171–179.
[57] L.C. Porter, F. Cervantes-Lee, H.H. Murray, Monatsh. Chem. 124 (1993) 775–782.
[58] R.A. Howie, T.C. Baddeley, J.L. Wardell, S.M.S.V. Wardell, J. Mol. Struct. 1020 (2012) 16–22.
[59] T.C. Baddeley, L. de S. Franca, R.A. Howie, G.M. de Lima, J.M.S. Skakle, J.D. de Souza, J.L. Wardell, S.M.S.V. Wardell, Z. Krist, Cryst. Mater. 224 (2009) 213–224.
[60] F.F. Jian, Y.F. Li, X.Y. Yang, P.S. Zhao, H.L. Ziao, Pol. J. Chem. 82 (2008) 1597.
[61] A.L. Amrutha Kala, K. Kumara, M. Prabhuswamy, G. Pavithra, K. Ajay Kumar, N.K. Lokanath, J. Med. Chem. Pharm. Chem. Comput. Chem. 8 (2016) 286–291.
[62] A.L. Amrutha Kala, K. Kumara, G. Pavithra, K. Ajay Kumar, N.K. Lokanath, Chem. Data Collect. 7-8 (2017) 107–115.
[63] H.-.K. Fun, K.V. Sujith, P.S. Patil, B. Kalluraya, S. Chantrapromma, Acta. Cryst E64 (2008) o1961–o1962.
[64] M.F. Simeonov, F. Fulop, R. Sillanpaa, K. Pihlaja, J. Org. Chem. 62 (1997) 5089–5095.
[65] X.-.S. Wang, J. Sheng, L. Lu, K. Yang, Y.-.L. Li, ACS Comb. Sci. 13 (2011) 196–199.
[66] M.A. Spackman, D. Jayatilaka, CrystEngComm 11 (2009) 19–32.
[67] M.J. Turner, J.J. McKinnon, S.K. Wolff, D.J. Grimwood, P.R. Spackman, D. Jayatilaka, M.A. Spackman, M.A. Crystal, Explorer, 17, University of Western Australia, Nedlands, Western Australia, 2017 http://hirshfeldsurface.net.
[68] B.S.A. Sasi, K.C. Bright, C. James, J. Mol. Struct. 1103 (2016) 286–294.
[69] Y. Erdogdu, D. Manimaran, M.T. Güllüoğlu, M. Amalanathan, I.H. Joe, S. Yurdakul, Opt. Spectrosc. 114 (2013) 525–536.
[70] V. Balachandran, G. Santhi, V. Karpagam, A. Lakshmi, Spectrochim. Acta A 110 (2013) 130–140.
[71] V. Balachandran, S. Lalitha, S. Rajeswari, Spectrochim. Acta A 97 (2012) 1023–1032.
[72] E. Scrocco, J. Tomasi, Adv. Quantum Chem. 11 (1978) 115–193.
[73] M. Szafran, A. Komasa, E. Bartoszak-Adamska, J. Mol. Struct. 827 (2007) 101–107.
[74] C.A. Lipinski, F. Lombardo, B.W. Dominy, P. Feeney, J. Adv. Drug Deliv. Rev. 23 (1997) 3–25.
[75] D.F. Veber, S.R. Johnson, H.Y. Cheng, B.R. Smith, K.W. Ward, K.D. Kopple, J. Med. Chem. 45l (2002) 2615–2623.
[76] N. Peela, D. Truong, H. Saini, H. Chu, S. Mashaghi, S.L. Ham, S. Singh, H. Tavana, B. Mosadegh, M. Nikkhah, Biomaterials 133 (2017) 176–207.
[77] W.Tapper Eccles, Cancer. Treat. Res. 155 (2010) 15–32.
[78] S.B. Nadin, L.M. Vargas-Roig, G. Drago, Cancer. Lett. 239 (1) (2006) 84–97.
[79] T. Tian, S. Olson, J.M. Whitacre, A. Harding, Integr. Biol. (Camb) 3 (1) (2011) 17–30.
[80] M.J. Wieduwilt, M. Moasser, Cell. Mol. Life Sci. 65 (10) (2008) 1566–1584.
[81] M. Scaltriti, J. Baselga, Clin. Cancer Res. 12 (2006) 5268–5272.
[82] D. Graus-Porta, R.P. Beerli, J.M. Daly, N.E. Hynes, EMBO J 16 (1997) 1647–1655.
[83] A. Citri, K.B. Skaria, Y. Yarden, Exp. Cell Res. 284 (2003) 54–65.
[84] P.J. Neuvonen, T. Kantola, K.T. Kivisto, Clin. Pharmacol. Ther. 63 (1998) 332–341.